Summer 6-22-2022

Observational constraints on the 520 km mantle discontinuity, mantle transition zone anisotropy, and local seismicity at Mount St. Helens

Han Zhang
Department of Earth and Planetary Sciences

Han Zhang

Candidate

Earth and Planetary Sciences

Department

This dissertation is approved, and it is acceptable in quality and form for publication:

Approved by the Dissertation Committee:

Dr. Brandon Schmandt , Chairperson

Dr. Jin Zhang

Dr. Peter Olson

Dr. Mousumi Roy

Observational constraints on the 520 km mantle discontinuity, mantle transition zone anisotropy, and local seismicity at Mount St. Helens

by

Han Zhang

B.S., Geophysics, University of Science and Technology of China, 2015
M.S., Earth and Planetary Sciences, University of New Mexico, 2018

DISSERTATION

Submitted in Partial Fulfillment of the
Requirements for the Degree of

Doctor of Philosophy
Earth and Planetary Sciences

The University of New Mexico
Albuquerque, New Mexico

August 2022

Acknowledgements

I would like to thank Dr. Brandon Schmandt for his visionary guidance through my M.S and Ph.D. periods. I have benefited from his incredible ability of decomposing complex questions into manageable projects. Moreover, his beautiful writing style impresses me a lot and serves as a shining example for me. I want to thank my committee members, Dr. Jin S. Zhang, Dr. Peter Olson, Dr. Tobias Fischer and Dr. Mousumi Roy for their professional input to these works and for their help in broadening my horizon. A special thanks to Dr. Mousumi Roy for her generous help in accommodating the committee requirement. I thank all my collaborators for their constructive suggestions and supervisions. I thank the geophysical group at the University of New Mexico for their help and companions during the happy and not-so-happy time. I also thank my host families Doris Buckman, Peter Snow, Lydia Congdon, and Dr. Roger Congdon for their selfless help during my time in Albuquerque. Lastly, I will always be grateful for my parents Xiaohong Zhang and Mingqiang Zhang, and my significant other, Lizzie Wu.

Observational constraints on the 520 km mantle discontinuity, mantle transition zone anisotropy, and local seismicity at Mount St. Helens

by

Han Zhang

B.S., Geophysics, University of Science and Technology of China, 2015
M.S., Earth and Planetary Sciences, University of New Mexico, 2018
Ph.D., Earth and Planetary Sciences, University of New Mexico, 2022

Abstract

Seismology provides valuable observational constraints to thermal and compositional states at inaccessible depths via understanding how elastic wave propagating through them. While many of fundament questions regarding solid Earth structures have been addressed during its more than 100 years history, some details remain unfilled and carefully designed approaches are needed to complete the pictures. This dissertation contributes observational constraints on three topics with newly developed methods. 1) We detected a controversial mantle discontinuity at about 520 km and concluded a mean mantle composition close to the Pyrolite model based on its seismic properties. 2) We isolated anisotropic effects in mantle transition zone from above and below the layer and hypothesized that concentrated mantle flow near slab gaps enhances local stress and aligns minerals at the depths. 3) We revisited hypocenter estimates of catalog earthquakes near Mount St. Helens and revealed similar depth distributions of the seismicity before and after its 2004-2008 eruption, suggesting a quick re-equilibrium of the magmatic system. These observations highlights seismology's role in advancing our understanding to various aspects of the Plate Tectonics.

Table of Contents

1. Introduction

Plate tectonics draws a big picture of how planet Earth sustains diverse environments via movements of rigid lithospheres over a mechanically weak asthenosphere layer. The theory explains many observed geologic features such as subductions of oceanic plates at convergent boundaries and formations of arc volcanoes above these subduction zones. The cooling of oceanic lithosphere after departing from mid-ocean ridge slowly densifies the layer and eventually makes it a heavier plate than the asthenosphere, which enables following subductions at trenches. When penetrating into the deep mantle, high temperature at depths melts volatile-rich layers of the subducting plate and therefore generates magma to feed the volcanos above it.

While the first-order explanations to these big picture topics are satisfying, some details are missing. For examples, we know that subducted slabs introduce thermal and compositional anomalies at depths, but the extents and spatial pattern of these variations are sparsely constrained. Moreover, uncertainty of these estimations grows with depth due to increasing limitation of direct samples. We are aware of the direction and rate of plate movements at surface thanks to modern geodesic measurements, but such knowledge on deep mantle convection remains poor. We know the ultimate magma source to feed the arc volcanoes, but detailed interactions between the shallow and deep magma system are under debate. To pave the way towards understanding these questions, multidisciplinary efforts at both observation and modeling sides are warranted.

Taking seismology as my primary field, I would like to contribute some seismic observational constraints on three topics here. The first one focused on detecting a controversial mantle discontinuity at ~520 km depth (520) and constraining its seismic

properties using data from more than 2,000 seismic stations across the contiguous United States. The 520 discontinuity is attributed to solid phase transition between wadsleyite and ringwoodite (olivine high pressure polymorphs), and therefore its strength could indicate the abundance of the associated minerals. The phase transition has a positive Clapeyron slope, which means a cooler temperature will elevate the discontinuity to a shallower depth. Consequently, the prevalence and seismic properties of the 520 offer valuable constraints on the olivine abundance and thermal anomalies at middle mantle transition zone depth. The study area covers a wide variety of tectonic settings extending from an active and long-lived subduction zone in the west across the cratonic interior to a passive eastern margin that has not experienced subduction since the Mesozoic. The enormous footprint enables detailed evaluations on the relationship between the observed 520's properties and past subduction processes. The results will improve our understanding of slab's role in altering mantle temperature and redistributing mantle materials. We presented 520's topography and S-wave contrast maps beneath the contiguous United States and compared them with predictions from modern mineral physics data. The estimated 520's properties suggested an up to 400 K temperature variations beneath the study region at transition zone depths and support a mean mantle composition close to the Pyrolite model.

The second contribution investigates the direction-dependent seismic velocities, i.e. anisotropy, inside a ~400-700 km deep layer beneath the Pacific Northwest of United States. Prevalence of seismic anisotropy at depths often indicates alignments of mantle minerals which were organized by shear stress resulted from mantle flow. Therefore, the direction and strength of seismic anisotropy could infer the current states of mantle convection when combining the observations with mineral physics measurements. The layer was assumed to

be isotropic due to the lack of adequate detection power and limited data from mineral deformation experiments. Here we paired seismic measurements from the top and bottom boundaries of the layer to isolate its contribution and utilized the non-linear relationship between phase amplitude and anisotropy strength to enhance the detection power. We presented new evidence of transition zone anisotropy without contrasting any previously obtained constraints using other methods. The findings extended observational constraints on mantle convection states to a deeper depth and therefore force a revisit of previous interpretations and associated modeling efforts. The spatial distribution of detected transition zone anisotropy overlaps with slab gaps suggested by recent tomographic results, which leads to our hypothesis of elevated shear stress near slap gaps resulting from focused mantle flow.

The last piece revisited the earthquake depths distribution of a decades-long local catalog at Mount St. Helens (MSH) after benchmarking the improved locations with a much denser temporary network. Hypocenter of volcanic earthquake is one of the most important indicators on where magmatic processes happen under an active volcano. Tracking the spatiotemporal changes of these hypocenters could infer changes in the magmatic system and therefore constrain its evolution history and potentially forecasts future hazard. However, at continuously monitored volcanos, changes in locating process and/or network geometry may introduce systematic bias to the hypocenter estimates. Consequently, a direct comparison of the catalog hypocenters over its long-time operation may be misleading. Here we developed a locating algorithm with 3D wavefront tracing and use the phase picks from the same local network (Pacific Northwest Seismic Network) to revisit the hypocenters estimates of seismicity near MSH from 1997 to 2022. The updated catalog eliminates an apparent change

in the depth distributions of seismicity before and after the 2004-2008 dome-building eruption of MSH and presents a more concentrate seismicity band between sea level and about 1 km above it. These results indicate that the dome-building eruption did not cause a long-lived reorganization of seismogenic structures near the top of the magmatic system.

2. Prevalence of a single 520 km discontinuity with pyrolitic seismic properties

2.1 Introduction

Bulk composition and temperature deep in the Earth control fundamental processes like solid convection and melting, which organize plate tectonics and may redistribute compositional variations through time. Due to extremely limited availability of direct samples, knowledge of mantle composition is largely shaped by boundaries that are detected by seismology and linked to specific phase or compositional transitions with properties predicted by mineral physics (Lay et al., 1998; Lebedev et al., 2002). Mantle transition zone seismic discontinuities and phase transitions of olivine polymorphs at about 400 - 700 km depth are among the most important indicators of an olivine-rich mantle (Ita and Stixrude, 1992; Frost, 2008). The 410 km discontinuity (410) represents the solid phase transition between olivine and wadsleyite, and the 660 km discontinuity (660) is primarily attributed to the decomposition of ringwoodite into bridgmanite and ferropericlase. However, multiple phase transitions are expected to contribute to changing seismic properties near the 660 (Hirose, 2002; Xu et al., 2008) and debate continues about whether it may be partly attributed to compositional changes across a leaky boundary in the mantle convection system (e.g., Deuss et al., 2006; Wu et al 2019; Waszek et al., 2021).

The intervening 520 km discontinuity (520) is commonly associated with the wadsleyite to ringwoodite transition (Shearer, 1996; Sinogeiken et al. 2003). It has a subtler seismic contrast, is more sporadically detected and, unlike the 410 and 660, it is not incorporated in widely used 1D reference Earth models (Deuss and Woodhouse, 2001; Julia and Nyblade, 2013; Tian et al., 2020; PREM from Dziewonski and Anderson, 1981; AK135

from Kennett et al., 1995). Additionally, some observations suggest that the 520 may split into two separate discontinuities or reflect the combination of the wadsleyite to ringwoodite phase transition and an exsolution of Ca-perovskite in areas of basalt enrichment (Deuss and Woodhouse, 2001; Saikia et al., 2008). Thus, the 520 remains a relatively uncertain structure despite its importance as a marker of the abundance of olivine polymorphs and potential enrichment of basalt in the mantle transition zone due to the long-term flux of subducting slabs, whose basaltic crust may separate from the depleted mantle lithosphere (Anderson and Bass 1986; Van Keken et al., 1996; Ballmer et al., 2015).

Relatively infrequent detection of the 520, compared to 410 and 660, may be largely attributed to challenges in resolution. Its subtler contrast and potentially wider depth interval weaken the 520's ability to generate distinct seismic phases and make its visibility more frequency-dependent than that of the 410. The low amplitude of seismic phases sensitive to the 520 often results in large uncertainties when estimating its properties and may lead to null detections under sparse sampling (Lawrence and Shearer 2006). Therefore, a carefully designed method targeting the 520 in a well-instrumented area is needed.

2.2 Data and Methods

Here, 520's detection and characterization are advanced using a Markov Chain Monte Carlo method to fit seismic receiver function data from more than 2,000 broadband seismometers across the United States simultaneously in several frequency bands (Fig. 2.1, A and B; Movie S1; Supplement Text). The method is applied to 64 caps with 300 km radius and the mean number of receiver functions per cap is >3,000. Their footprint covers a wide variety of tectonic settings extending from an active and long-lived subduction zone in the

west across the cratonic interior to a passive eastern margin that has not experienced subduction since the Mesozoic (Seton et al., 2012). Inversions using parameterizations with and without the 520 enable statistical evaluation of its spatially varying significance and seismic properties. Moreover, pairing the estimated 520 properties with those of the 410 provides insights to vertical heterogeneities and therefore allows a 3D evaluation of the potential thermal and chemical anomalies in the transition zone.

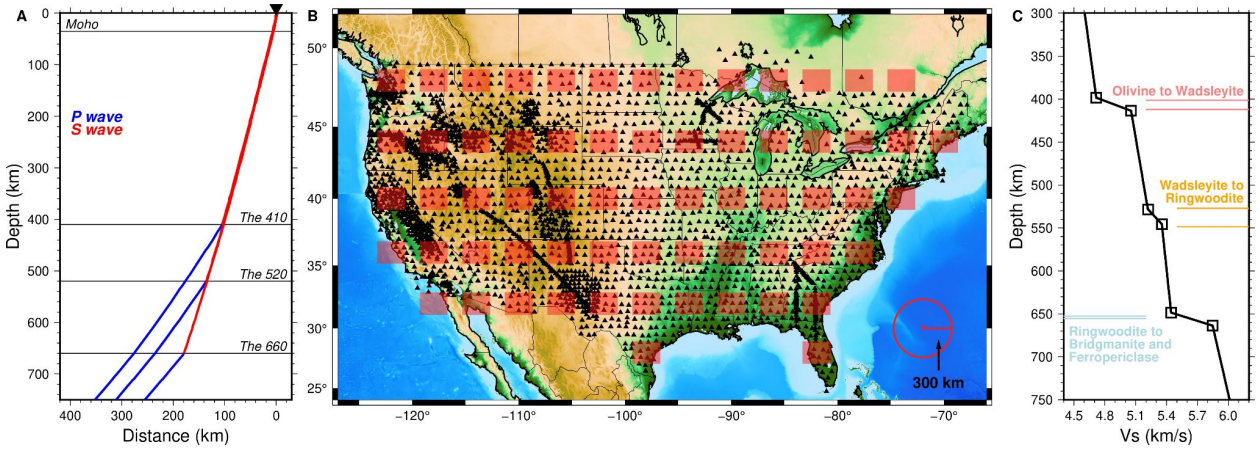

Figure 2.1 Teleseismic P-to-S ray path sampling and model parameterization. (A) Teleseismic ray paths of P-to-S conversions at transition zone discontinuities. (B) Map of seismic stations (black triangles) labeled with the center of caps used for sub-array stacking. (C) The parameterization of the shear wave velocity in the depth window of interest. The depth range of the phase transitions between Olivine high pressure polymorphs are represented by colored horizontal bars.

Our null hypothesis is that adding a 520 discontinuity does not significantly improve the goodness of fit to the observations. When parametrizing the forward models, we used four parameters to define a discontinuity as an enhanced linear velocity gradient (Fig. 2.1C; Supplement Text). Two parameters correspond to the Vs and depth at the top and bottom of each discontinuity, respectively. Consequently, the models have 12 parameters when including three discontinuities and 8 parameters when only including the 410 and the 660.

The second parameterization forms a subset of the first and therefore a ratio of Residual Sum of Squares (RSS) between the two parameterizations indicates the significance of a 520. The RSS is defined as

$$RSS = \sum_{i,j} \left(\frac{obs_{i,j} - syn_{i,j}}{\sigma_{i,j}} \right)^2$$

where *obs* and *syn* represent the observed and synthetic waveforms respectively. The σ is the observational uncertainty. Index *i* and *j* are for sample points and frequency bands, respectively. Assuming the random noise follows a normal distribution, an F-test requires

$$\frac{RSS2}{RSS1} \geq 1 + \frac{p1 - p2}{ndf - p1} * finv(1 - \alpha, p1 - p2, ndf - p1)$$

to reject the null hypothesis at a confidence level of 1-α. The *p1* and *p2* are the number of model parameters, which are 12 and 8 respectively. The *ndf* stands for the number of degrees of freedom, which is estimated to be 46 (Supplement Text). The *finv* is the inverse of cumulative F-distribution function, with inputs of the probability, numerator degrees of freedom, and denominator degrees of freedom.

2.3 Results and Discussion

The RSS ratio map and two waveform examples support a widespread 520 (Fig. 2.2). The F-test requires an RSS ratio greater than 1.31 to reject the null hypothesis at 95% confidence. About 84% (54 out of the 64 caps) of the area surpass the threshold and therefore require a 520 to better fit the observed waveforms. The results are consistent with an olivine-rich mantle where the wadsleyite to ringwoodite phase transition is nearly ubiquitous. The null detections are limited to a narrow north-south band where the tomographically inferred subducting Juan de Fuca slab reaches transition zone depths (Schmandt and Lin, 2014, Fig.

2.S1). While a low olivine fraction could explain its apparent absence, destructive stacking of the 520 signal arising from misrepresented velocity anomalies or striking phase transition topography may also diminish the observed 520 signal.

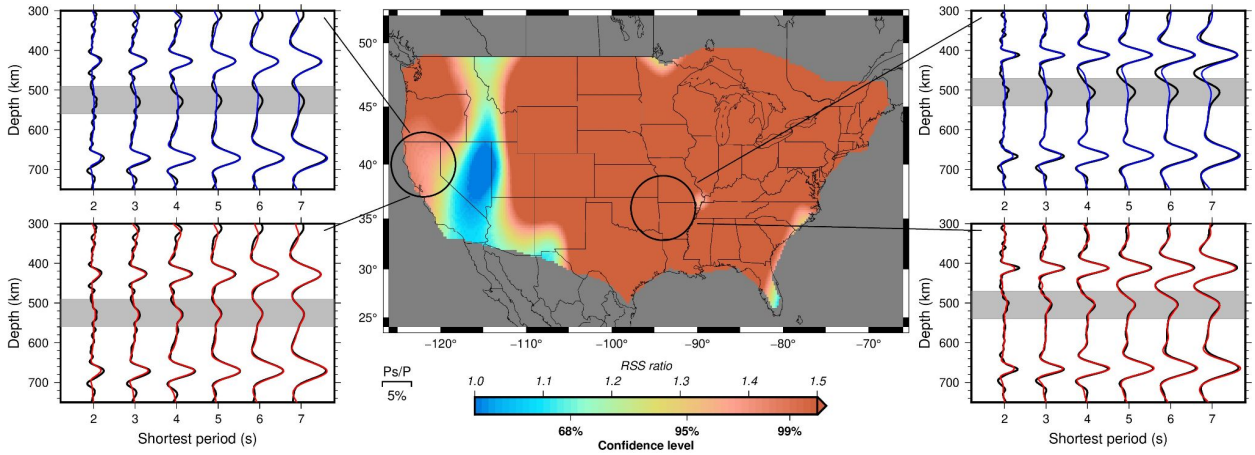

Figure 2.2 The RSS ratio map and waveform examples of requiring a 520 discontinuity. The confidence level for the requirement of a 520 is marked by the bottom side of the color scale. In the waveform examples, the observations are shown as black lines. The synthetic waveforms from inversions without a 520 are in blue and those from inversions with a 520 are in red. The shaded region highlights waveform fit improvement after including a 520.

Previously reported splitting of the 520 discontinuity (Deuss and Woodhouse, 2001; Tian et al., 2020), i.e. a 560 km discontinuity (560), is not a significant feature in our results (Fig. 2.2 and 2.S2). The exsolution of Ca-perovskite from majorite garnet is hypothesized to create the 560 and therefore its visibility may reflect concentrations of subducted oceanic crust near the bottom of transition zone (Saikia et al., 2008). The absence of deeper detections at ~560 km in this study indicates that the shallower wadsleyite-ringwoodite transition is more important to fitting P-to-S conversions across the study area. Consequently, it appears that basaltic crust is not sufficiently concentrated in the mid-transition zone to make Ca-perovskite exsolution the dominant phase transition. Given the long history of

subduction beneath the western margin of North America, the new results favor entrainment of slab crust to greater depths, localized near the bottom of the transition zone or extending into the lower mantle (e.g., Ballmer et al., 2015).

Discontinuity depths further support that the wadsleyite-ringwoodite transition is the dominant cause of the 520 (Fig. 2.3B and 2.S3; Supplement Text). The 520 depths from the positive detections (95% confidence) have a mean of 506 km with a standard deviation of 10 km. Despite that the depths are generally shallower than the 520 km implied by its name, they agree well with modern mineral physics predictions of 500-514 km for the wadsleyite to ringwoodite transition within 50 K of a normal adiabat (Tsujino et al., 2019; Zhou et al., 2022; Fig. 2.4B). Moreover, a mean depth slightly shallower than 520 km is consistent with previous seismic detections at both global and regional scales (~510 km in Tian et al., 2020, ~515 km in Julia and Nyblade, 2013).

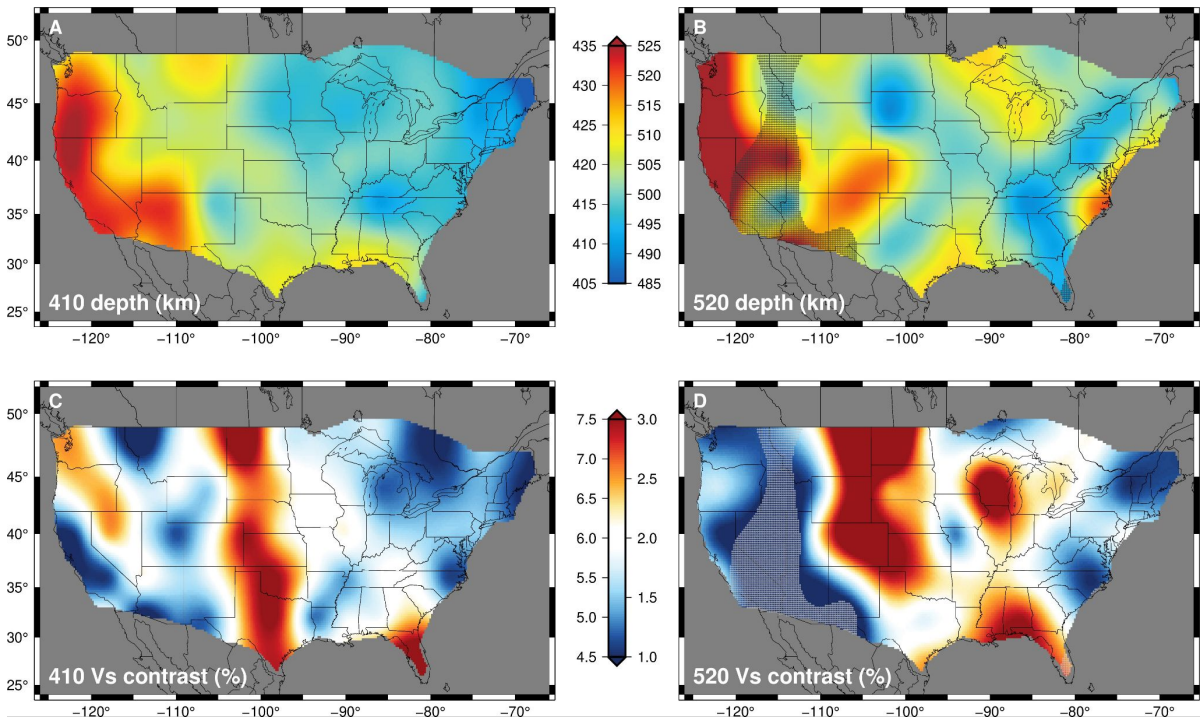

Figure 2.3 Depths and Vs contrast of the 410 and the 520 discontinuities. The mesh pattern in panel B and D is taken from the RSS map in figure 2, indicating regions where a 520 is not required at 95% confidence.

The proximity of the shallower olivine-wadsleyite transition associated with the 410 serves as a useful reference for more detailed evaluations of the 520 (Fig. 2.3). The depths of the 520 and 410 show a strong positive correlation coefficient of 0.68 (Fig. 2.4A). Temperature and hydration levels are the major influences on the depths of the two phase transitions (Inoue et al., 2010). Since both transitions have positive Clapeyron slopes (Katsura et al., 2004; Suzuki et al., 2000; Inoue et al., 2006), similar thermal variations near the two discontinuities would predict positively correlated topography consistent with our results. In contrast, varying hydration levels would predict anti-correlated topography because increasing water content elevates the 410 and depresses the 520 (Inoue et al., 2010). Our estimated slope between the 520 and the 410 depths ranges from 0.9 to 1.5 at 95% confidence, with a best fit value of 1.2 (Fig. 2.4A; Supplement Text). The estimated slopes generally agree with mineral physics predictions using a ratio of the two Clapeyron slopes

(0.8-1.3 from Inoue et al., 2006; 1.4-2.0 from Suzuki et al., 2000), indicating a dominant role for thermal anomalies in altering 410 and 520 topography. For Clapeyron slope estimates of 4.1-6.9 MPa/K, the observed 45 km variation would correspond to lateral temperature variations of 230-390 K.

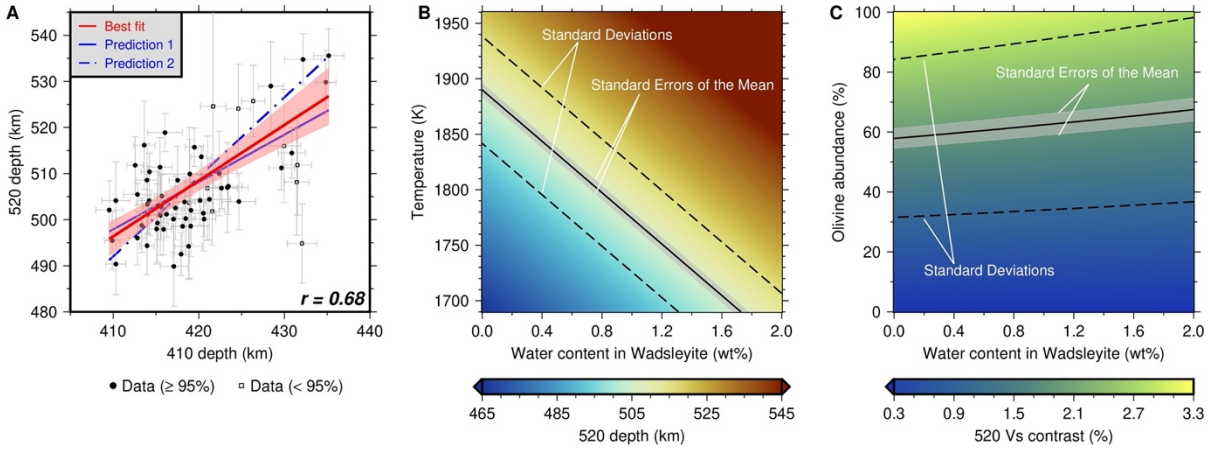

Figure 2.4. Comparison of mineral physics predictions and seismic observations. (A) Observed 520 and 410 depths and a best fit model with 95% confidence level (red). The correlation coefficient is denoted by the lower-right corner. Mineral physics predictions on the slope are shown as blue lines. Prediction 1 uses Clapeyron slopes from Katsura et al., (2004) and Inoue et al., (2006). Prediction 2 uses Clapeyron slopes from Katsura et al., (2004) and Suzuki et al., (2000). (B) Temperature and hydration effects on the predicted 520 depth. The solid black line shows the observational mean 520 depth. The gray region shows the standard error of the mean depth and the dashed black lines show its standard deviation. (C) Olivine abundance and hydration effects on the predicted 520 Vs contrast. The solid black line shows the mean Vs contrast at 520. The gray region shows the standard error of the mean contrast and the dashed black lines show its standard deviation. Mineral physics data were taken from Zhang and Bass (2016) and Zhou et al., (2022).

Given the evidence that the 520 represents the wadsleyite-ringwoodite transition, the abundance of olivine polymorphs should primarily control the magnitude of its Vs contrast, with more minor effects due to hydration levels. The observed 520 Vs contrasts from all caps have a mean of 1.9% with a standard deviation of 0.9% (Fig. 2.4C). Horizontal variability in Vs contrasts generally shows higher values beneath the central United States and lower

values near the eastern and western margins (Fig. 2.3, C and D). The results could reflect lateral variations in the abundance of olivine polymorphs, with a more olivine-enriched transition zone beneath the continental interior. However, many factors including uncertainty of heterogeneous 3D velocity and attenuation may influence variations among individual sub-array estimates of the 520 Vs contrast, so we focus on estimating mean olivine abundance. The standard error on the mean 520 contrast is 0.1% so a one-sigma range on the mean contrast is 1.8%-2.0%. Assuming a water partitioning ratio between wadsleyite and ringwoodite of 2:1 and an Fe# number of 7.6 in wadsleyite (Inoue et al., 2010; Ishii et al. 2018; Zhou et al., 2022), the mean Vs contrast range is consistent with an olivine abundance of 54%-61% under dry conditions (Fig. 2.4C). Incorporating 1.0 wt% water into wadsleyite increases the estimates to 58%-66%.

2.4 Conclusions

The range of olivine abundance estimated from the mean Vs contrast at 520 is similar to the 56% abundance in the pyrolite model (Green and Fallon, 1998; Frost, 2008). Scarcity of evidence for basalt enrichment in the study area, which would favor a more prominent 560 and a less prominent 520 than we found (Saikia et al., 2008), is consistent with an olivine-rich composition like pyrolite. The widespread presence of a single 520 consistent with a normal mantle geotherm and near-pyrolite olivine abundance suggests that while the seismic signals from the 520 are subtler than those of the 410 and 660, the olivine-wadsleyite transition can be a valuable marker of mantle physical state where adequate seismic resolution exists. Here, the properties of the 520 indicate that the relevance of the olivine-rich pyrolite model of the upper mantle extends to mid-transition zone depths.

2.5 Supplementary

Data processing

We extracted three components (P-SV-SH) Ps receiver functions from collected broadband waveform data in the contiguous U.S. using a multi-channel deconvolution method (Mercier et al., 2006). We then filtered the SV component data at six different frequency bands, namely 2 s - 15 s, 3 s - 15 s, 4 s - 15 s, 5 s - 30 s, 6 s - 30 s, and 7 s - 30 s. We converted the time-domain receiver functions to depth-domain via raytracing the Ps phase in an existing 3D tomographic model (Schmandt and Lin, 2014).

We grouped the receiver functions in 300 km caps based on their piercing points at 500 km depth and stacked them in depth-domain to form a multiband dataset. The 300 km radius cap maintains a minimum trace number of 1000, which promises a decent signal to noise ratio of phase amplitude on the order of about 3% assuming the incoherent noise decay by a factor of square root of trace numbers. Grouping the data at 500 km depth increases the coherence of the P-to-S conversions and strengthens the detection power of the 520. The observational uncertainties of the stacked receiver functions were estimated using bootstrap resampling with 200 iterations.

Model parameterization

Our parameterization of the input shear wave velocity structure at transition zone depths is shown in Fig 2.1C. We fixed the absolute S-wave velocity at 300 km and 750 km depths using values from an existing body wave tomography model (Schmandt and Lin, 2014). We then used four parameters – depth, absolute Vs at the beginning and end of each

linear transition – to define a discontinuity as an enhanced linear gradient. The P-wave velocity was scaled from the Vs structure using the ratios from the same tomographic model. The density was scaled using ratios in AK135 (Kennett et al., 1995). The seismic structures above 300 km and below 750 km, including the Moho depth, were taken from the tomographic model as well.

Parameters conversion

The model parameters were converted to discontinuity depths and Vs contrast for a direct comparison with mineral physics data (Fig. 2.S3). We calculated the discontinuity depths by averaging the depths at the top and bottom of a linear gradient. We calculated the Vs contrast by extrapolating the velocity gradients above and below the discontinuity to the expected depth and reported a fractional velocity jump at the depth.

Markov Chain Monte Carlo inversion

Movie 2.S1 shows an animated example of the Markov Chain Monte Carlo inversion process.

We used a reflectivity code to calculate synthetic receiver functions (Levin and Park, 1997) from a forward model and matched the slowness distribution of the observed data during the stack process (Munch et al., 2018). The path integrated attenuation effects were corrected using the structure from PREM (Dziewonski and Anderson, 1981).

With the observational data, their uncertainties, and an effective forward modeling algorithm (Levin and Park, 1997), we adopted a Markov Chain Monte Carlo (MCMC)

inversion method to form posterior distributions of the model parameters. Following Bissig et al., (2021), we chose a likelihood function in a format of

$$L = \exp\left(-0.5 * RSS/N\right)$$

where N stands for the total number of points when calculating the Residual Sum of Squares (RSS). Our prior distributions of model parameters are uniform functions spanning a plausible range of mantle transition zone seismic properties (Table 2.S1). We used the Metropolis–Hastings algorithm to draw samples with Gaussian probability density functions. The standard deviation of the depth Gaussian function is 1.5 km while that of the absolute Vs Gaussian function is 0.015 km/s. Such steps offer 30% to 50% acceptance rate during the inversion. For each region, we run the MCMC with 100,000 iterations (4 chains times 25,000 iterations per chain). We used the high performance clusters at the Center for Advanced Research Computing in the University of New Mexico to parallelize the process and the computation took ~25,000 CPU hours.

While the best one model from a probabilistic inversion may vary from one trial to another, the averaged parameters represent more stable estimates (Bodin et al., 2012; Shen et al., 2013). Here, we choose to average the best 200 models because it focuses on highly successful models while providing enough samples to calculate standard deviations.

We tested the algorithm by inverting synthetic receiver functions from a pyrolite composition along mantle adiabat with a potential temperature of 1600 K (Xu et al., 2008; Wang et al., 2018; Fig. 2.S4). The input model contains the three phase transitions between olivine polymorphs in the depths of interest. They are olivine to wadsleyite transition near 410 km, wadsleyite to ringwoodite transition near 540 km, and the decomposition of ringwoodite into bridgmanite and ferropericlase near 660 km (Fig. 2.S4A). Other than these

phase transformations within olivine high pressure polymorphs, the gradual and nonlinear transition from majorite garnet to bridgmanite also contribute to the velocity gradient at depths greater than ~640 km (Fig. 2.S4A). The overlap of multiple phase transitions complicates the structure of the 660 discontinuity and may invalidate our parameterization of one linear gradient. However, this simplification should not interfere with the primary goal of this study, which is to determine the significance of the 520 across the study area.

The MCMC inversion fits the major characteristics of the receiver function waveforms in all the six different frequency bands (Fig. 2.S4B). The recovered depths and Vs contrasts for the 410 and the 520 agree with the input values from the two corresponding phase transitions (Fig. 2.S4, C and D), indicating that the linear parameterization works for simple structures. However, while the inverted 660 depth is similar to the value from the ringwoodite transition, the Vs contrast is much larger and clearly incorporates contributions from the majorite transition (Fig. 2.S4A). Such a result suggests that a more sophisticated model parameterization is needed to associate seismic properties of the 660 with specific phase transitions. Here, we focus on the 520 and 410 because each is associated with phase transition between olivine polymorphs, which can be effectively modeled with our simple parameterization.

Number of independent samples

We calculated the synthetic receiver functions from preferred model parameters and subtracted them from the observations to form waveform residuals. We then estimated the number of degrees of freedom (*ndf*) using equations 25-31 in Walsh et al., (2013). The estimated *ndf* from the 64 caps range from 32 to 62 with an average value of 46 (Fig. 2.S5).

While it is straightforward to use the estimated *ndf* from each region separately, we preferred to use one value for all the regions. Because the data were processed identically and averaged all source-receiver pairs in equal size areas, we expected similar numbers of degrees of freedom across the array. Therefore, we performed the F-test using an *ndf* of 46 for all regions.

York fit to the 520 and 410 depths

We used a York fit to find a linear model to explain the observed 520 and 410 depths (York et al., 2004; Fig. 2.4A). The uncertainties of the depth estimates were used to weight the data. In Fig. 2.4A, we report the best fit model and a 95% confidence region of the model.

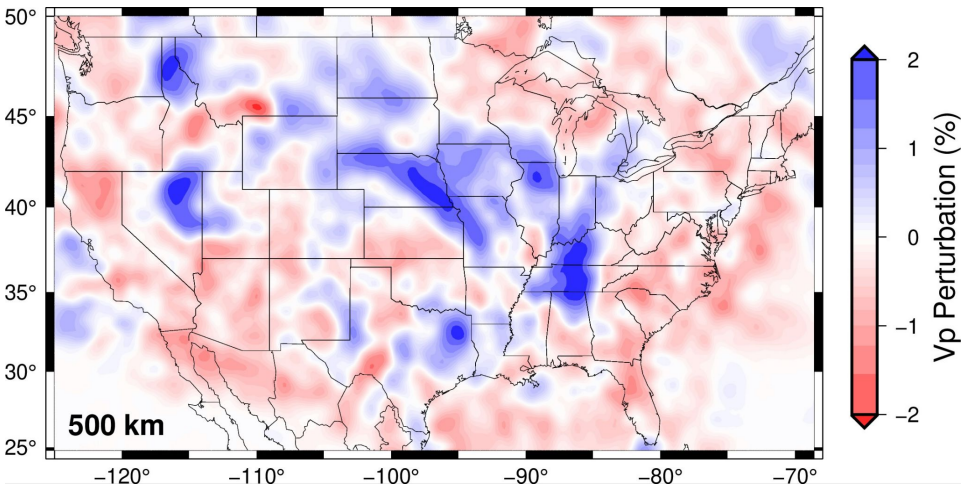

Figure 2.S1 P-wave velocity perturbation at 500 km depth. The tomography model is from Schmandt and Lin (2014).

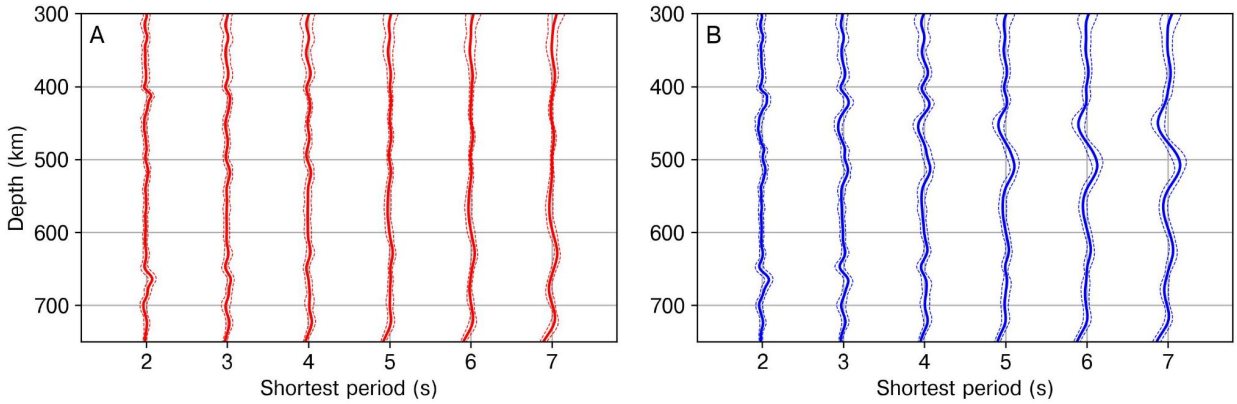

Figure 2.S2 Stacked multiband receiver function residuals. (A) Residuals from inversions with a 520. The dashed lines mark the standard deviations. (B) same as A but for residuals from inversions without a 520.

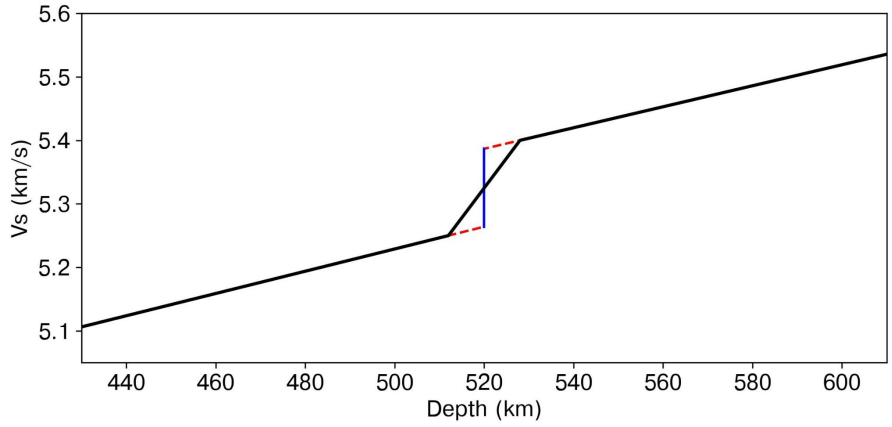

Figure 2.S3 Example of converting model parameters to discontinuity depth and Vs contrast.

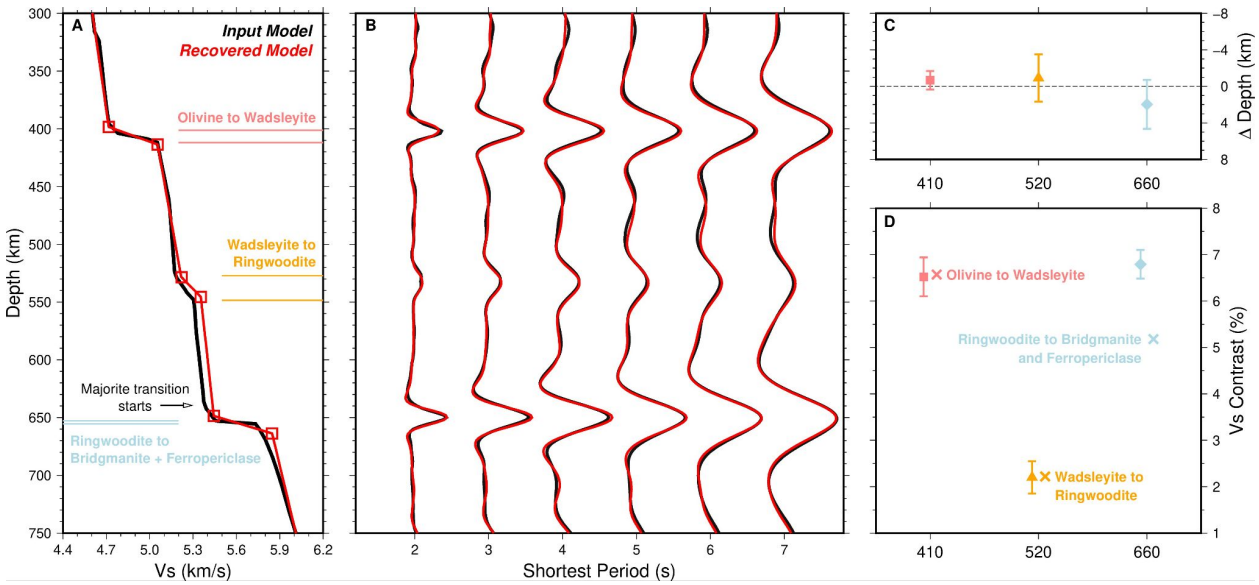

Figure 2.S4 Algorithm test with pyrolite synthetics. (A) The input (black) and recovered (red) Vs structures between 300 km and 750 km depths. The depth range of the phase transitions between Olivine high pressure polymorphs are represented by colored horizontal bars. The start depth of the Majorite to Bridgmanite transition is marked by a black arrow. Its end depth is off the figure at ~780 km. (B) The input (black) and recovered (red) receiver function waveforms at six frequency bands. This panel shares the same y-axis with panel A. (C) The recovered discontinuity depths. The phase transition depths are set at zero and the differential depths are plotted. A positive value means the inverted depth is deeper than the input, so the y-axis is reversed. (D) The input and recovered Vs contrasts. The phase transition values are denoted as colored Xs. The error bars represent the standard deviations of the posteriors.

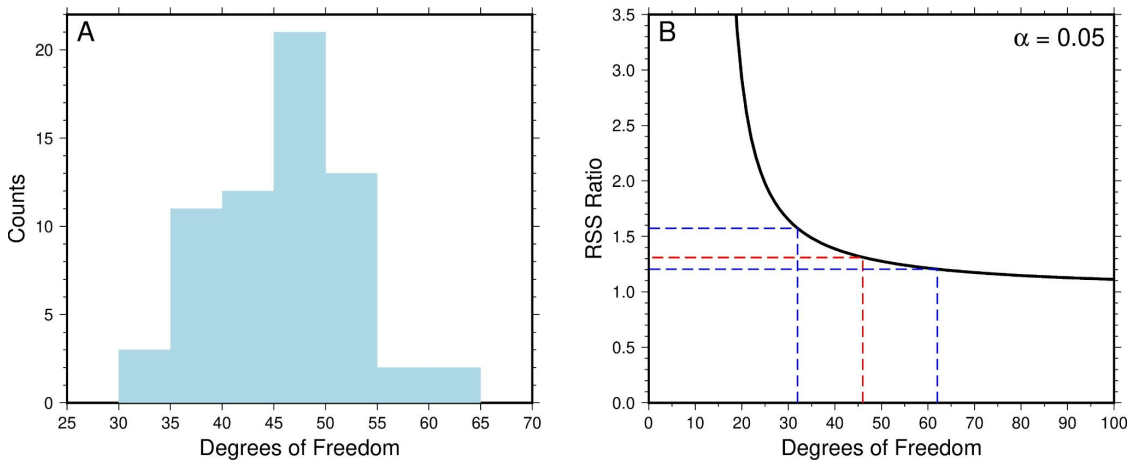

Figure 2.S5 Estimated number of degrees of freedom and required RSS ratio by an F-test at 95% confidence. (A) The distribution of the estimated number of degrees of freedom from the 64 regions. (B) The required RSS ratios at a confidence level of 95%. Our preferred number of independent samples is 46 and is denoted with the red dashed line. The two blue dashed lines represent the minimum and maximum degrees of freedom from the 64 caps.

	410	520	660
Depth (km)	350-470	470-570	570-750
Vs Contrast (%)	Positive	Positive	Positive
Width (km)	Positive	0-60	Positive

Table 2.S1 Prior distributions of model parameters.

rfs_mcmc_rank035.mp4

(https://drive.google.com/file/d/1IBxS5Kwxd_-wYfy6PGgLuc0vHkGPHFum/view?usp=sharing)

Movie 2.S1 An animated example of the MCMC inversion process. (A, B) Comparison between observed and synthetic receiver functions at multiple frequency bands. The observed receiver functions are shown as black waveforms. The synthetic receiver functions from inversions with and without a 520 are shown as red and blue waveforms, respectively. (C) The RSS values variations from inversions with (red squares) and without (blue triangles) a 520 as a function of acceptance number. The RSS ratio between the two model parameterizations are shown as orange dots. (D, E) The averaged discontinuity depths and Vs contrasts of the 410 and the 520 and their associated standard deviations from the best 200 models.

3. Localized anisotropy in the mantle transition zone due to flow through slab gaps

3.1 Introduction

Seismic anisotropy of Earth's mantle provides important insights into convective flow and composition at inaccessible depths. There is abundant evidence for concentrated anisotropy at depths within a few hundred kilometers of the mantle's top and bottom, but the prevalence of anisotropy at intermediate depths is more uncertain (Long & Becker, 2010). Potential reasons for diminished anisotropy in the transition zone and most of the lower mantle include decreasing anisotropy of higher-pressure olivine polymorphs (Mainprice 2015; Zhang et al., 2018), strain partitioning into localized shear zones (Girard et al., 2016), and accommodation of strain by diffusion creep rather than dislocation creep (Mohiuddin et al., 2020; Ritterbex et al., 2020). Depth-integrated measurements of mantle anisotropy like teleseismic shear wave splitting (SWS) are often assumed to be dominated by anisotropy at depths less than ~300 km. This perspective is supported by the positive correlation of fast-axis orientations with plate tectonic deformation and surface wave azimuthal anisotropy (Becker et al., 2012; Long & Becker, 2010), as well as isolated evidence that local deep earthquakes exhibit SWS comparable to teleseismic measurements (Fischer & Wiens, 1996). However, some long-wavelength global imaging studies and regional attempts to separate near-source contributions to path-integrated SWS suggest anisotropy extending to mantle transition zone depths of about 400-700 km (Huang et al., 2019; Lynner & Long, 2015; Yuan & Beghein, 2013).

The Pacific Northwest (PNW) of the U.S. is well-suited to investigate the depth distribution of mantle anisotropy (Fig. 3.1a). Active subduction is thought to organize

vigorous mantle flow, the region has been densely instrumented with broadband seismometers, and a large depth-integrated anisotropy signal is indicated by spatially averaged teleseismic SWS measurements (Liu et al., 2014; Long et al., 2012; Supporting Information S1) (Fig. 3.1c). Surface wave azimuthal anisotropy constrains regional anisotropy at depths less than about 200 km, but that depth interval can only account for about half of the anisotropy indicated by SWS (Lin et al., 2011; Wagner & Long, 2013). Recent attempts using finite-frequency *SKS* splitting intensity tomography suggest up to 8% anisotropy at 200-400 km to accommodate the remaining signal (Mondal & Long, 2020). However, the amplitude of the sensitivity kernels reduces with depth, leaving uncertainty about anisotropy at >400 km depth. Recent full-waveform inversion (FWI) for anisotropic velocities using regional earthquakes suggests that subduction-driven flow beneath the PNW creates anisotropy at transition zone depths (Zhu et al., 2020). The fast orientations from FWI tomography generally agree with SWS, but the depth-integrated magnitude of anisotropy is much smaller than that obtained by SWS. Thus, it is unclear how much transition zone anisotropy is needed to explain the large depth-integrated SWS signals in the PNW.

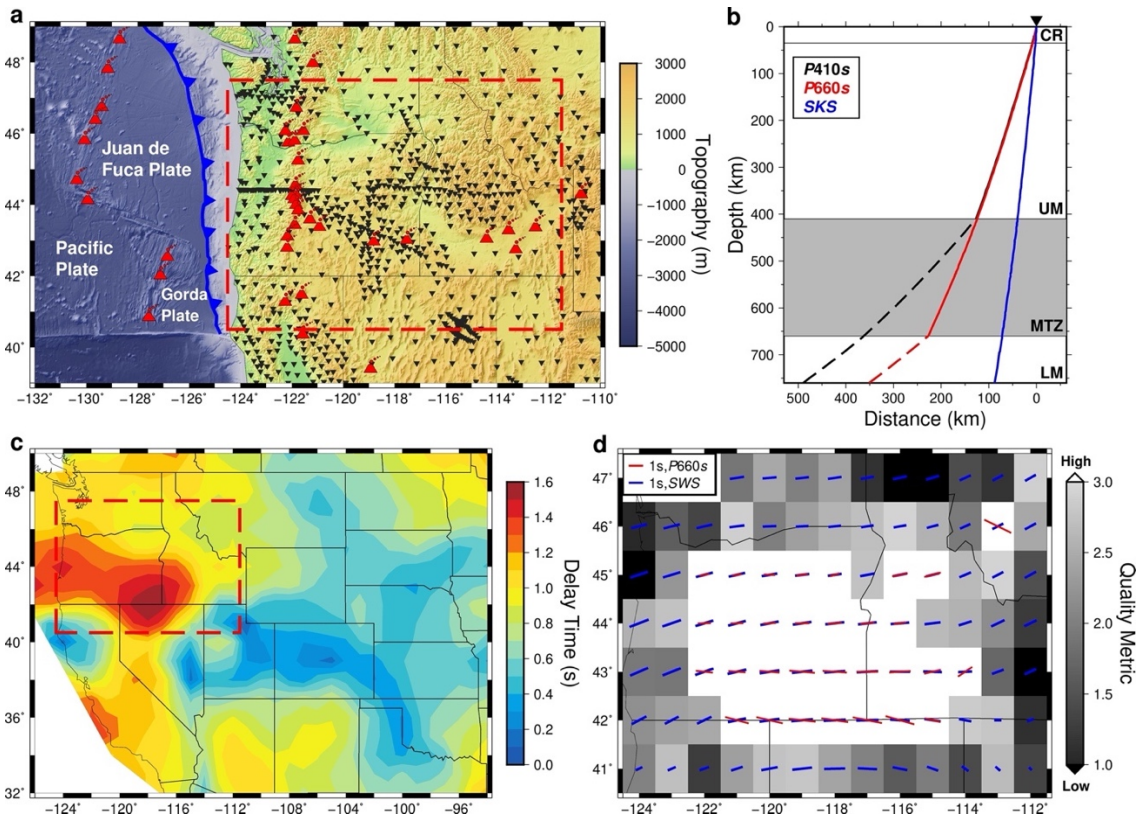

Figure 3.1 Tectonic setting of the PNW and seismic observations of anisotropy. (a) The Juan de Fuca Plate is actively subducting beneath the PNW. Holocene volcanoes (red symbols) and broadband seismometers (black inverse triangles) are superimposed on the topography. The red dashed box outlines our study area. (b) Ray paths of the *P*410*s* (black), *P*660*s* (red) and *SKS* (blue) phases. Compositional layers are labeled: crust (CR), upper mantle (UM), mantle transition zone (MTZ), and lower mantle (LM). (c) Spatially averaged SWS delay times (Liu et al, 2014) in the western U.S. The red dashed box outlines our study region. (d) Comparison between our estimated splitting parameters from the *P*660*s* (red bar) and the spatially averaged SWS results (blue bar). The grayscale background indicates the quality of the estimations from the *P*660*s*.

3.2 Data and Method

This study takes advantage of teleseismic P-to-S (*Ps*) conversions at the boundaries of the mantle transition zone to isolate potential deep contributions to anisotropy beneath the PNW. The two converted phases, *P*410*s* and *P*660*s*, almost share ray paths in the upper mantle so the paired observations can localize signals from within the transition zone (Fig. 3.1b). In an isotropic mantle with 1-D velocity structure, *Ps* conversions would only be

observed with P-SV polarization. But constructive anisotropy along the shear wave ray path can cause splitting effect, leading to observations of *Ps* energy on SH polarization. We collected broadband waveform data from teleseismic earthquakes with magnitude greater than 5.5. For data with P wave signal-to-noise ratio (SNR) greater than 3, we extracted 3-component (P-SV-SH) receiver functions using a multimode frequency domain deconvolution method (Mercier et al., 2006). The receiver functions were filtered using a zero-phase bandpass filter between 0.07 Hz and 0.25 Hz and corrected for normal moveout by extracting velocities along the ray paths within a previous tomographic model (Schmandt & Lin, 2014).

Since small delay times often yield undetectable *Ps* signal on the SH component (Montagner et al., 2000), stacking many waveforms is often required and attempts to use the two phases are limited to areas with strong anisotropy (Vinnik & Montagner, 1996; Kong et al., 2018). Based on their piercing points at 500 km depth, we stacked the receiver functions that sample the transition zone in 200 km radius caps. We choose a 200 km radius because it is the minimum necessary to achieve stable receiver function stacks in our study region. A bootstrap resampling-based quality metric was used to determine regions with adequate SNR to constrain transition zone anisotropy (Fig. 3.1d; Supporting Information S2). The region with adequate *P*660*s* signals corresponds well with the area of large SWS delay times (>1.3 s, Fig. 3.1c). The splitting parameters, fast-axis orientation and delay time, estimated from *P*660*s* using transverse energy minimization (Long & Silver, 2009; Walsh et al., 2013) also share great similarity with the SWS results, indicating that most of the anisotropic signals can be explained at depths above the 660 (Fig. 3.1d). The mean difference of the fast-axis orientation estimates is 6.1˚ with a standard deviation of 11.8˚, and the mean difference of

delay times is -0.03 s with a standard deviation of 0.34 s. However, the transverse component energy minimization approach to measuring anisotropy results in large delay time uncertainties (~0.5 s) for the *P*410*s* and *P*660*s* estimations at individual stacking points, so they are not optimal for constraining the potentially weak anisotropy in the transition zone.

The amplitude ratio of the conversions between the two shear wave components (P_{SH}/P_{SV}) provides greater sensitivity to the magnitude of anisotropy than the delay time as the strength of anisotropy increases (Fig. 3.2). Due to this non-linear sensitivity, differences in the P_{SH}/P_{SV} amplitude ratios between *P*660*s* and *P*410*s* may constrain transition zone anisotropy with less uncertainty than splitting times. Because of the two *Ps* phases naturally share the same back-azimuth, pairing them during the measurement should eliminate the back-azimuth component from the anisotropic effects and enhance statistical detection power compared to separate measurements (Supporting Information Text S3). The measurement of amplitude ratios of the two stacked *Ps* phases is similar to the conventional method of measuring splitting intensity for the *SKS* phase (Chevrot, 2000). The splitting intensity is defined as the amplitude ratio of the *SKS* phase between the transverse component and the time derivative of the radial component. In contrast, we measured the amplitude ratio of the stacked *Ps* phase between the time integrated SH component (P_{SH}) and original SV component (P_{SV}). Mathematically, the derivative and integration processes offer identical results after removing the integration constant. The integration process we adopted here preserves the one-sided polarity of the P_{SV} phase, which simplifies the measurements (Fig. 3.2).

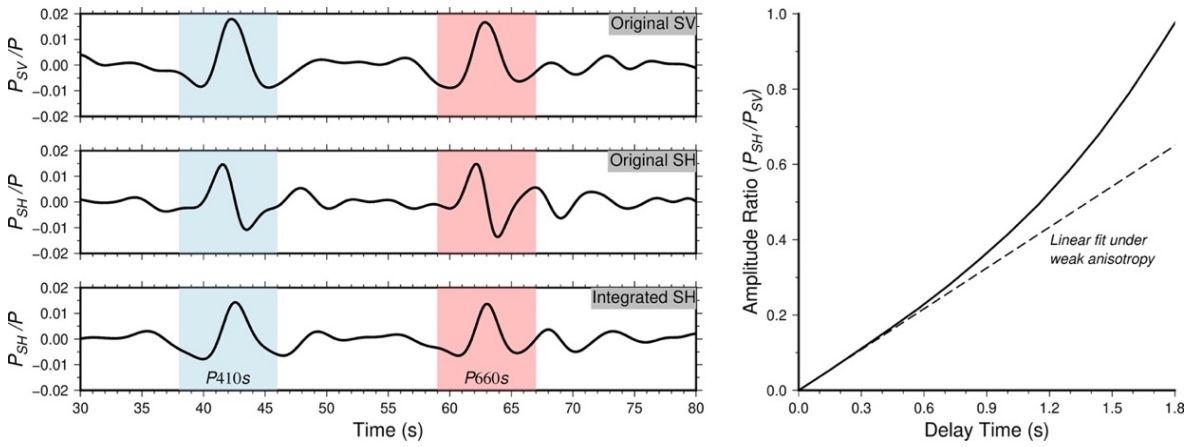

Figure. 3.2 Synthetic receiver function from an anisotropic upper mantle model and the relationship between the P_{SH}/P_{SV} amplitude ratios and delay times. The amplitude ratio P_{SH}/P_{SV} is measured as the peak shear wave amplitude on the integrated SH component divided by that on the original SV component. The amplitude ratios are approximately proportional to the delay times under weak anisotropy. At moderate anisotropy, the amplitude ratios become increasingly sensitive to the magnitude of anisotropy.

We again measured the amplitude ratios using stacks in 200 km radius caps and applied bootstrap resampling to assess the uncertainty (Supporting Information S3). After correcting the polarity shift using fast orientation estimated from the *P*660*s* from energy minimization, we stacked the receiver functions from all available back-azimuths and slownesses. Since such processes were applied to *P*410*s* and *P*660*s* simultaneously, the two stacked phases still share the same back-azimuth effect. Although individual P_{SH}/P_{SV} amplitude ratio varies with back-azimuth, the pairing prevents such variation and better isolates anisotropy within the transition zone. A null hypothesis of an isotropic transition zone and all anisotropy above the 410 would predict indistinguishable amplitude ratios from the two phases. Consequently, any significant differences between the P_{SH}/P_{SV} ratios measured from the two stacked phases should indicate transition zone anisotropy.

3.3 Results and Discussion

We used the Cohen's distance (Cohen, 2013), i.e. the standardized differences, between the two amplitude ratio distributions and the corresponding paired t-test to evaluate the significance of transition zone anisotropy (Supporting Information S3). About half of the resulting Cohen's distances show a significant difference at 68% confidence (±1.0), with a few locations exceeding the 95% confidence level (±2.0) (Fig. 3.3, b and d, See Fig. 3.S1 for more examples).

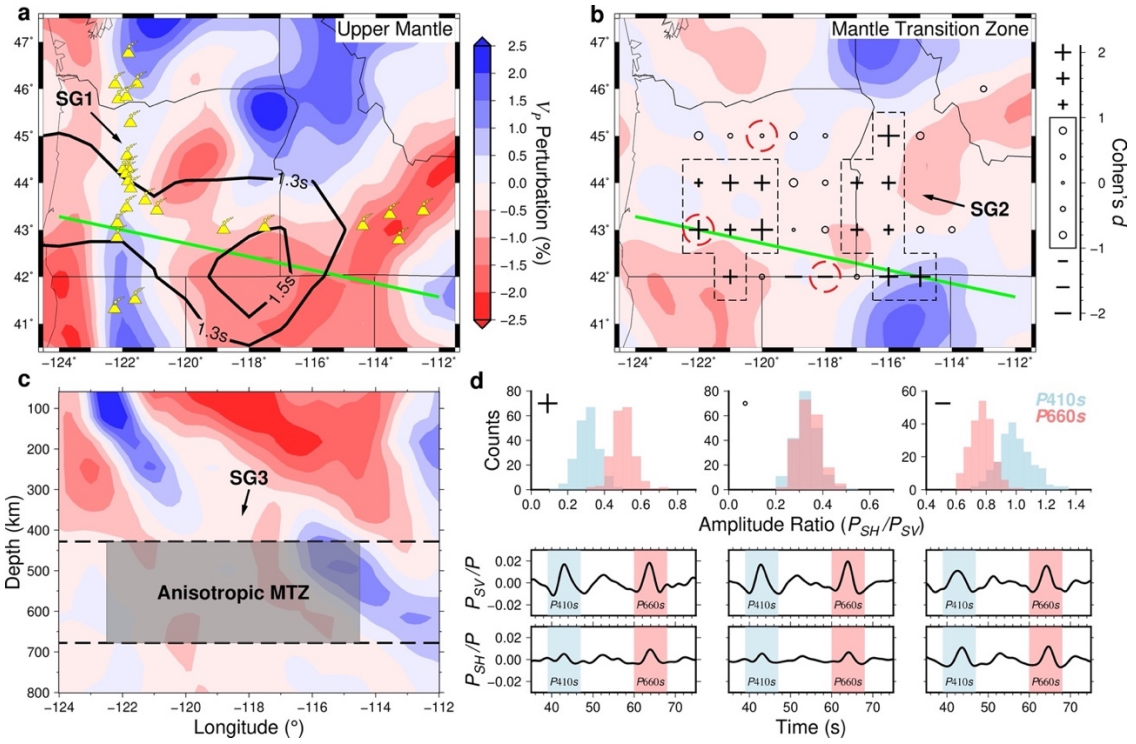

Figure. 3.3 Seismic tomography of the study region and amplitude ratio evidence for anisotropy. Depth averaged V_P perturbation within (a) the upper mantle (60-350 km) and (b) the mantle transition zone (435-635 km) from Schmandt and Lin (2014). The positions of slab gaps are labeled by SG. Holocene volcanoes (yellow symbols), contoured spatially averaged SWS delay times (1.3s and 1.5s, black lines), and observed Cohen's distances are superimposed on the tomography. (c) Cross section of the V_P perturbation beneath the green line on the maps. The gray box outlines where mantle transition zone (MTZ) anisotropy is required by the observations. (d) Examples of the observed amplitude ratios and stacked waveforms from the locations with red dashed circles in panel b. The amplitude ratios from the *P*410*s* are in red while those from *P*660*s* are in blue. The amplitude ratio distributions come from bootstrap resampling.

We defined three categories for the observed results: constructive interference where *P*660*s* amplitude ratios are greater than *P*410*s* amplitude ratios (labeled '+'), destructive interference where *P*410*s* amplitude ratios are greater than those of *P*660*s* (labeled '-'), and neutral where there is no significant difference (labeled '○'; Fig. 3.3b). The neutral observations fail to reject the null hypothesis of an isotropic transition zone. Two larger areas of constructive interference and one smaller area of destructive interference indicate localized transition zone anisotropy inboard of the Cascades volcanic arc (Fig. 3.3c).

The two constructive interference areas exhibit greater path-integrated anisotropy from the 660 to the surface compared to that from the 410 to the surface. Such observations can be fit with a common fast orientation for an anisotropic layer extending through the upper mantle and into the transition zone. Both constructive interference areas lie within gaps between high-velocity slab fragments identified by seismic tomography (Schmandt & Lin, 2014; Hawley & Allen, 2019) (Fig. 3.3, a and b, labeled SG). The western area is located near an along-strike slab gap in the upper mantle beneath the central to southern Oregon backarc region that is hypothesized to focus mantle flow beneath backarc volcanic provinces (Hawley & Allen, 2019). The eastern area of constructive interference is located between two high-velocity features interpreted to be older slab fragments located further beneath the continental interior (Liu & Stegman, 2011; Schmandt & Humphreys, 2011). The southern edge of the eastern constructive interference area appears to overlap the position of the high-velocity slab beneath northern Nevada.

Two stacking points that exhibit destructive interference of transition zone and upper mantle anisotropy are located at the southern edge of the well-resolved area (Fig. 3.3b). Destructive interference of splitting within the transition zone and above it due to changing

fast orientation with depth can create a larger P_{SH}/P_{SV} amplitude ratio of the *P*410*s* compared to that of *P*660*s* (Fig. 3.S2; Supporting Information S4). Given the small area that exhibits destructive interference and the tradeoffs among estimating the thickness, fast orientation, and magnitude of anisotropy for the two layers, we refrain from further interpretation of these two stacking points.

Anisotropy within the transition zone could arise on account of lattice preferred orientation (LPO) of olivine polymorphs. Our interpretation focuses on potential LPO origins because most of the constructive observations lie in normal mantle, as opposed to slab fragments, based on tomographic imaging (Fig. 3b). Contributions from shape preferred orientation may be more important to consider where subducted slabs are sampled. Wadsleyite is the stable polymorph of olivine in the upper transition zone and has a maximum single-crystal shear wave anisotropy of ~9% (Zhang et al., 2018). The peak anisotropy is smaller than that of olivine above the 410 (Fig. 3.S3), but deformation experiments have successfully produced up to 2% anisotropy of wadsleyite (Kawazoe et al., 2013; Ohuchi et al., 2014). At lower transition zone depths, the stable polymorph of olivine is ringwoodite and it is elastically almost isotropic at transition zone pressures (Mainprice, 2015). Therefore, it is unlikely to contribute to the observed anisotropic signals. Atypical anisotropic minerals formed near or within the subducted slab may contribute to anisotropy. At relatively low mantle temperatures, two strongly anisotropic minerals, phase E and akimotoite, could form at transition zone depths (Hao et al., 2019; Satta et al., 2019). Phase E is a reaction product between olivine and water at upper transition zone depths (Satta et al., 2019). Akimotoite is enriched in the refractory harzburgitic lithosphere of the slabs at lower transition zone depths (Ishii et al., 2019). Both minerals have single-crystal shear wave

anisotropy up to ~20%, which makes them alternative candidates for the origin of observed anisotropic signals in the transition zone.

The deformation mechanisms for the mantle transition zone minerals depend on many factors, such as temperature, flow stress, strain rates, and grain size. The laboratory determined glide-driven dislocation creep of transition zone minerals can cause development of LPO (Kawazoe et al., 2013). However, a recent theoretical study suggests that deformation in the mantle transition zone is dominated by climb-driven dislocation creep, which does not develop LPO (Ritterbex et al., 2020). The glide-driven dislocation creep is favored by high stress and strain rates in the laboratory, whereas typical flow stress and strain rates in the ambient mantle are several orders lower. Therefore, the development of LPO may be expected only in areas of stress concentration, such as where mantle flow is focused through constrictions (Alisic et al., 2012; Király et al., 2020).

Based on the mineral physics' constraints, we constructed three types of forward models to illustrate a range of potential anisotropic structures (Fig. 3.4a; Supporting Information S5). The simplest model includes only upper mantle anisotropy extending from the Moho to 400 km depth, such that anisotropy is consistent with only an olivine LPO origin (Fig. 3.4a, #1). Since there is no anisotropy within the transition zone, the first model can explain the neutral observations where the P_{SH}/P_{SV} amplitude ratios from the *P*660*s* and *P*410*s* are indistinguishable.

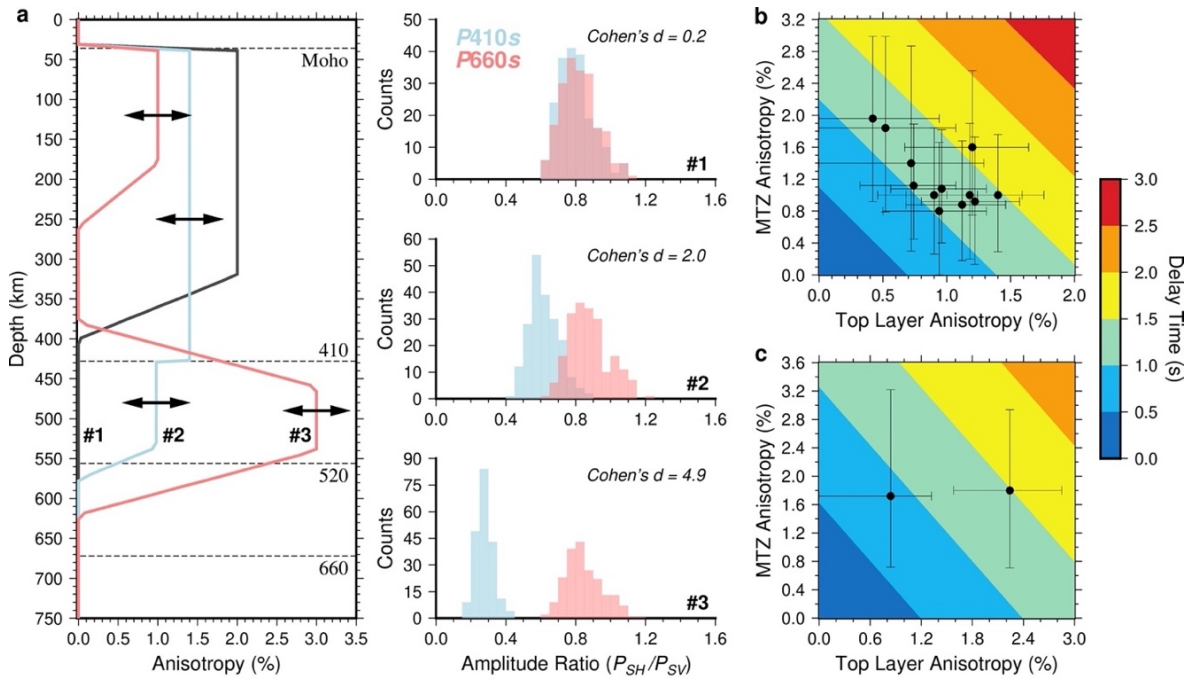

Figure. 3.4 Forward models and the inverted mantle transition zone anisotropy. (a) Three types of forward models (#1-3) and their corresponding amplitude ratios distributions. The Cohen's distances are denoted by the histograms. (b) Inverted mantle transition zone (MTZ) anisotropy for most of the constructive interference areas using parameterization of model #2. The error bar represents the 68% confidence intervals. The color background represents the delay time from a vertically propagated shear wave. (c) Inverted results for the two stacking points in the southeastern corner using parameterization of model #3.

The second model also contains upper mantle anisotropy, but it is underlain by an anisotropic layer in the upper part of the transition zone where wadsleyite is stable (Fig. 3.4a, #2). This model yields constructive interference of transition zone and upper mantle splitting effect and then offers a plausible explanation for places with a larger *P*660*s* amplitude ratio. With this model parameterization, we used a grid search of upper mantle and transition zone anisotropy magnitudes to find the best model for explaining the observations (Supporting Information S6). Using a ray parameter and back-azimuth distribution identical to the observational data, the inverted results show that inclusion of ~1-2 % anisotropy in the upper

mantle transition zone can reproduce the observed differences between the two amplitude ratios for most stacking points exhibiting constructive interference (Fig. 3.4b).

The third model is built on the idea that subducted slab is present in the transition zone, thus atypical minerals which are not expected in the ambient mantle may contribute to anisotropy (Fig. 3.4a, #3). In this case, the anisotropy within the transition zone is allowed to extend to deeper depths where wadsleyite is no longer stable. The deeper anisotropy may arise from akimotoite associated with the cool slab fragment, such as beneath the southeastern corner of the well-resolved area (Fig. 3.3b). When modeling the two stacking points in the southeastern corner, the additional thickness of the anisotropic layer prevents requiring unreasonably large anisotropy in the wadsleyite stability field (Fig. 3.4c).

The three anisotropic structures suggest various geodynamic settings (Fig. 3.5). The first model represents upper mantle flow due to absolute plate motion and subduction zone corner flow in the shallow upper mantle. In this conventional context, anisotropy is primarily due to olivine LPO created by flow-induced dislocation creep. The second model requires focused mantle flow caused by slab ruptures as hypothesized by prior geodynamic modeling of regional mantle flow and anisotropic fast orientations (Zhou et al., 2018). If flow through slab gaps induces locally high stress at transition zone depths, the LPO of wadsleyite could contribute a portion (up to 0.4 s in this study) of the total splitting delay time. The additional anisotropy at transition zone depths helps explain the large discrepancy between estimated splitting delay times from surface wave azimuthal anisotropy studies and observed teleseismic SWS in the central Cascades backarc (Wagner & Long, 2013). The third model represents the potential influence of compositional heterogeneity due to a slab fragment at

transition zone depths, which is a scenario that may be even more important for subduction zones with older and colder slab fragments in the transition zone.

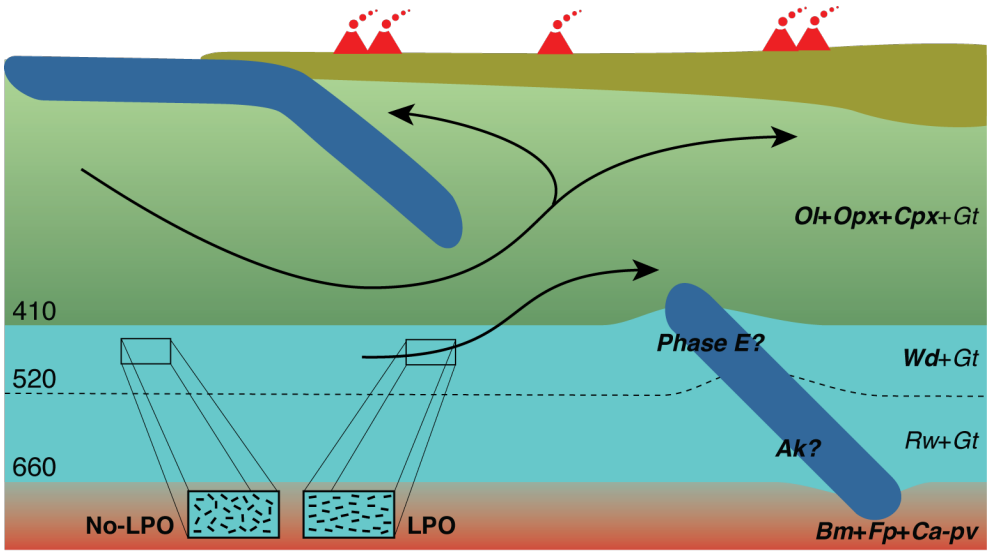

Figure. 3.5 Schematic model of flow going through slab gap. The rupture of a continuous slab induces enhanced flow near the slab gap. The resulting flow concentrates stress and develops lattice preferred orientation (LPO) of anisotropic minerals at transition zone depths. Common minerals are labeled using italic font with anisotropic minerals in bold: olivine (Ol), orthopyroxene (Opx), clinopyroxene (Cpx), garnet (Gt), wadsleyite (Wd), ringwoodite (Rw), bridgmanite (Bm), ferropericlase (Fp), Ca-perovskite (Ca-pv), akimotoite (Ak).

3.4 Conclusions

The new results support the potential development of seismic anisotropy at mantle transition zone depths, with magnitudes that can be similar to those in the upper mantle. However, in contrast to upper mantle anisotropy that is observed ubiquitously, it appears that transition zone anisotropy may be restricted to areas of locally high stress such as focused flow through fragmented slabs.

3.5 Supporting information

Text S1

The teleseismic shear wave splitting (SWS) measurements were first averaged at each station using circular averaging (Montagner et al., 2000). Then we created a $1^{\circ} \times 1^{\circ}$ grid dataset by averaging the station-based SWS measurements in a 200 km radius bin.

Text S2

The transverse energy minimization method uses a grid search framework to find the splitting parameters, fast-axis orientation and delay time, to minimize the energy of the SH component within a target time window (Long & Silver, 2009). The grid intervals for our fast-axis orientation and delay time are 1˚ and 0.1 s, respectively. The time windows were set as ± 4 s from the peak amplitude of the *Ps* phase on the stacked SV component. After finding the global minimum, under the assumption of Gaussian noise, it is conventional to report the uncertainty of the estimate using an F-test formulation (Walsh et al., 2013). Here we reported the 95% confidence level of our estimates.

However, given the fact that the noise may not follow a Gaussian distribution, the grid search results from low SNR phases (e.g. *P*410*s* and *P*660*s*) often suffer from an artificial global minimum unless further quality control is applied. We adopted a bootstrap based metric to qualify the reliability of the estimates based on how much they reduce the amplitude of the corrected SH stack compared to the raw SH stack (Fig. 3.1d). The metric was defined as

$$M = (RMS_{zero} - RMS_{min})/SD_{boot}$$

where the RMS_{zero} stands for the root-mean-square (rms) value of a zero-lag time SH stack, RMS_{min} is the rms value from the minimum energy parameters. SD_{boot} is the standard

deviation of the rms values from 200 bootstrap resamples of the target SH window. A larger *M* means greater rms reduction and suggests a more reliable global minimum. Examples with various *M* values can be found in Fig. 3.S4. Fig. 3.1d only gives the estimates from the *P*660*s* phase with *M* greater than 3.

Text S3

Since the *P*410*s* and *P*660*s* phases are much weaker than the *SKS* phase, stacking receiver functions from different azimuths is required to obtain stable measurements. Synthetic tests indicate that the polarity of the *Ps* phases on the SH component changes when the back azimuth crosses the fast- or slow-axis of anisotropy (Fig. 3.S5). Therefore, to prevent destructive interference of traces from different azimuths during stacking, we flipped the SH traces in the 2nd and 4th quadrants using the fast-axis orientation estimated from the *P*660*s* phase. The flip was applied to both *Ps* phases because the null hypothesis of an isotropic mantle transition zone (MTZ) suggests that the two *Ps* phases share the same fast-axis orientation.

The amplitude ratio was then measured as the peak shear wave amplitude on the integrated stacked SH component over that on the stacked SV component (hereinafter referred to as P_{SH}/P_{SV}). Theoretically, under weak anisotropy (delay time less than a tenth of a period), individual P_{SH}/P_{SV} amplitude ratio is proportional to the delay time in a format of $0.5*\sin2(\beta-\varphi)*\delta t$ (Montagner et al., 2000). Consequently, the stacked amplitude ratio is also proportional to the delay time in an approximate format of $0.5*\delta t*\sum|\sin2(\beta-\varphi)|/n$. The || represents absolute value function and n is the number of receiver functions.

Synthetic tests demonstrate that the positive correlation continues to moderate anisotropy (delay time up to one third of a period), where the amplitude ratio becomes increasingly sensitive as the magnitude of anisotropy increases (Fig. 3.2). Although a simple formula is not available due to the non-linearity, the amplitude ratio should still represent a product of the summed back-azimuth effect and the path-integrated delay time. Because the *P*410*s* and *P*660*s* naturally share the same back-azimuth distribution, the null hypothesis of an isotropic transition zone would predict indistinguishable amplitude ratio measurements from the two *Ps* phases. Please note that such prediction is independent to our choice of pre-known fast-axis orientation when we flipped the SH receiver functions, as long as the *P*660*s* and *P*410*s* phases were flipped simultaneously.

Bootstrap resampling, with 200 samples, was used to assess the uncertainties of the amplitude ratios assuming a normal distribution of the resampled stacks. The bootstrap resampling provides empirical distribution function of our estimations and the central limit theorem justifies the assumption of normality. The paired Cohen's distance was calculated using the following equation

$$Cohen's\ d = (\overline{AmpR_{660}} - \overline{AmpR_{410}})/SD_{diff}$$

where $\overline{AmpR}$ is the mean of measured amplitude ratios for the *P*410*s* and *P*660*s* phase, and SD_{diff} is the standard deviation of the two groups' difference. The usage of the standard deviation of groups' differences – rather than the pooled standard deviation – arises from the fact that these two phases are paired. Using the corresponding paired 2-sample t-test, a two-tailed 68% confidence level would require Cohen's distance either greater than 1.0 or smaller than -1.0. A two-tailed 95% confidence level sets thresholds at ±2.0. The observed Cohen's distances were superimposed on the tomographic map in Figure 3.3b.

We want to note that the amplitude ratios measured here are not sensitive to isotropic velocity anomalies or attenuation structures, because they are the ratios between two components of one seismic phase. Moreover, the agreement between the splitting parameters measured from *P*660*s* and *SKS* suggest anisotropy, rather than discontinuity topography, as the major contributor to the energy on the SH components.

Text S4

We explored the effects of two anisotropic layers with different fast-axis orientations using synthetic data (Fig. 3.S2; Supporting Information S7). The anisotropy in the top layer (36 – 320 km) is 2.5%, and that of the bottom layer (360 – 556 km) is 1.5%. Accordingly, the delay times from the two layers are ~1.3 s and ~0.5 s respectively. The fast-axis orientation of the upper layer was fixed at 89˚, which is the mean fast-axis orientation estimated from the *P*660*s* phase (Fig. 3.S5).

Since the top layer dominates the depth-integrated anisotropic effect, the fast-axis orientation estimations from the energy minimization method show no significant difference with the 95% confidence intervals. Such results suggest the fast-axis orientation measurements are not ideal to constrain differential orientations if the common layer dominates the total anisotropic effect. In contrast, the delay times show greater variations with respect to the differential orientations, but are still less sensitive when compared with the Cohen's distances.

Increasing the differential orientation between the two layers moves the resulting Cohen's distances from a constructive interference area (0˚ - 30˚) to a neutral area (40˚ - 60˚), and finally to a destructive interference area (70˚ - 90˚). Such results provide an alternative fit

to the neutral observations and a potential explanation for the destructive observations in Fig. 3.3b.

Text S5

To illustrate a range of possible anisotropic structures beneath our study region, we constructed three types of forward seismic models in Fig. 3.4a. Note that the back-azimuth and slowness distributions for the forward calculations were identical to those in other observational measurements to properly account for the effects of the specific source-receiver pairs available in the study area. Several constraints were taken from prior seismic models, mineral physics data, and our observations here from *P*660*s*. Firstly, the depths of mantle discontinuities come from previous migration results (Zhang & Schmandt, 2019). The depth-integrated delay time from the three models were set to match the mean estimated delay time from the *P*660*s* in the best resolved regions (light background in Fig. 3.1d), which is 1.4 s (Fig. 3.S6). Such a setting makes the three models indistinguishable from *SKS* data alone.

Moreover, from bottom to top, we listed the detailed constraints in each layer below.

Lower mantle

- The agreement between the splitting parameters from the *P*660*s* and SWS suggests an isotropic lower mantle (Fig. 3.1d), which applies to all three models.

Mantle transition zone

1. As a control group, there is no transition zone anisotropy in model #1.
2. At the ambient mantle, mineral physics data suggested a nearly isotropic lower transition zone layer even lattice preferred orientation of ringwoodite was developed

(Fig. 3.S3). Therefore, model #2 has an isotropic lower MTZ layer. We further assumed a uniform upper MTZ layer with gradual transition at the 520 for simplicity.

3. When slab is present in the transition zone, atypical minerals such as phase E and akimotoite may contribute to the recorded anisotropic signal. Therefore, the deeper anisotropic layer in model #3 is set to match the depth extent (~380 km to ~620 km) of the slab suggested from tomographic results (Fig. 3.3c).

At the 410

1. As a control group, there is no anisotropy near the 410 in model #1.
2. At the ambient mantle, mineral physics data suggested a ~30% anisotropy drop across the 410 in a pyrolite model, which comes from the lower intrinsic elastic anisotropy of wadsleyite compared with olivine (Fig. 3.S3). Under the assumption of simple shear deformation from mantle flow, the ~30% drop was honored in model #2.
3. When slab is present in the transition zone, the deformation may not follow the simple shear assumption. Therefore, we didn't implement any constraints at the 410 in model #3.

Upper mantle

- Surface wave studies in this region suggest ~1-2% azimuthal anisotropy within the first ~200 km (Wagner & Long, 2013), which applies to all three models. Due to the poor depth resolution in the upper mantle of our data, and for the sake of simplicity, we further assumed a uniform anisotropy strength in the upper mantle layer for all three models.

Crust

- There is no clear evidence of strong crustal anisotropy so we set it to be zero for simplicity.

While there are countless models that are consistent with the observational constraints, depth resolution is inadequate to constrain detailed structure. So, we consider three models to highlight potential anisotropy contributions from the upper mantle above 410 km, the upper transition zone where wadsleyite is stable, and the lower transition zone. The detailed parameters of our models are listed below.

1. Model #1 only contains an anisotropic layer extending from the Moho (at 36 km) to 400 km. The strength of anisotropy is 2.0% from the Moho down to 320 km and then linearly decreases to 0% at 400 km. The 80 km gradual transition avoids strong artificial P-to-S conversions on the synthetics, which were not found in observational receiver functions.
2. Model #2 has a uniform anisotropic layer from the Moho down to the 410 discontinuity (at 428 km), which is underlain by another uniform layer of anisotropy in the upper MTZ (428-556 km). The strength of anisotropy in the upper mantle layer is 1.4% and that of the upper MTZ layer is 1.0%. The ~30% drop in the strength across the 410 discontinuity comes from the mineral physics constraints mentioned before. A 40 km thick 520 discontinuity (at 556 km) was set to avoid strong artifacts.
3. Model #3 has two separated anisotropic layers. The top layer (Moho-260 km) has a strength of 1.0% while the deeper one (380-620 km) has a maximum strength of 3.0%. To avoid artifacts from sharp contrast, the lower boundary of the top layer and the two boundaries of the second layer have gradual transitions over 80 km.

Using synthetic receiver functions (Supporting Information S7), Figure 3.4a and 3.S6 give the distribution of the amplitude ratios and the estimated splitting parameters from the three models.

Text S6

We used a grid search method to invert preferred models for explaining the observed amplitude ratios. At each stacking point, we used noise-free synthetics with a ray parameter and back-azimuth distribution identical to the observation. Such a process ensures the magnitudes of anisotropy within the two layers are the only factors affecting the amplitude ratios.

In the model #2 parameterization, the top layer has a uniform anisotropy between the Moho and 320 km depth. The second layer starts from 400 km and extends down to 556 km. The 30% anisotropy drop across the 410 (at 428 km) is kept in the second layer. From 320 km to 400 km, a gradual transition between the two layers was applied to avoid strong artifacts. The two magnitudes used in the grid search are the uniform anisotropy in the top layer and the maximum anisotropy in the upper transition zone layer (Fig. 3.4a, #2).

In the model #3 parameterization, the top layer extends from the Moho to 260 km. The second layer starts at 380 km and extends to 620 km. Gradual transitions over 80 km at the boundaries are applied. The two magnitudes in grid search are the maximum anisotropy within the two layers (Fig. 3.4a, #3).

The P_{SH}/P_{SV} of the $P410s$ and $P660s$ phases from each of the models were calculated using noise-free synthetics. The two standardized squared deviations from the observed means were summarized as a misfit term.

$$Q = (\Delta AmpR_{410}/SD_{410})^2 + (\Delta AmpR_{660}/SD_{660})^2$$

where $\Delta AmpR$ is the difference between observed and predicted amplitude ratios for the $P410s$ and $P660s$. SD is the standard deviation of observed amplitude ratios. Given the assumption of normally distributed amplitude ratios, the misfit term Q approximately follows a chi-square distribution with a 2 degrees of freedom (Fig. 3.S7). Accordingly, the 68% confidence intervals of our best fit model were reported using the chi-square distribution in Fig. 3.4, b and c.

When interpreting the inverted magnitudes of anisotropy in the upper mantle and transition zone layers, please keep in mind that only the depth-integrated anisotropy in each layer is constrained rather than the magnitude of anisotropy at a specific depth. Consequently, there is a tradeoff between the strength and thickness of anisotropy within either the upper mantle or transition zone. The upper mantle layer is thicker, so the potential tradeoff is larger. For instance, if anisotropy were concentrated in only a 100 km depth interval of the upper mantle (e.g., mantle lithosphere or asthenosphere), then the actual magnitude of anisotropy would be locally greater than our estimates. The tradeoff may span a smaller range of values in the transition zone layer because it is thinner. For a pyrolite composition, almost all anisotropy is expected in the wadsleyite stability field from about 410 to 520 km (Fig. 3.S3). We consider it less likely that only a subset of the wadsleyite depth interval contains anisotropy because it is smaller and does not include major

rheological contrasts. Thus, the optimized values for the transition zone layer are a more localized constraint on the actual magnitude of anisotropy (Fig. 3.4, b and c).

Text S7

The synthetic receiver functions were generated using a reflectivity method (Levin & Park, 1997). Identical to the processes applied on the observed data, the synthetic receiver functions were rotated to the P-SV-SH coordinate and were filtered between 0.07 Hz and 0.25 Hz. We then contaminated the synthetics with pre-event noise collected from observed USArray data. We assumed a P wave SNR of 5 when adding the noise to the synthetics. Normal moveout correction was applied to the synthetics using the input velocity model. Using a ray parameter and back-azimuth distribution identical to the whole PNW dataset, the noisy synthetics produce the forward modeling results in Fig. 3.4a, Fig. 3.S2 and Fig. 3.S6.

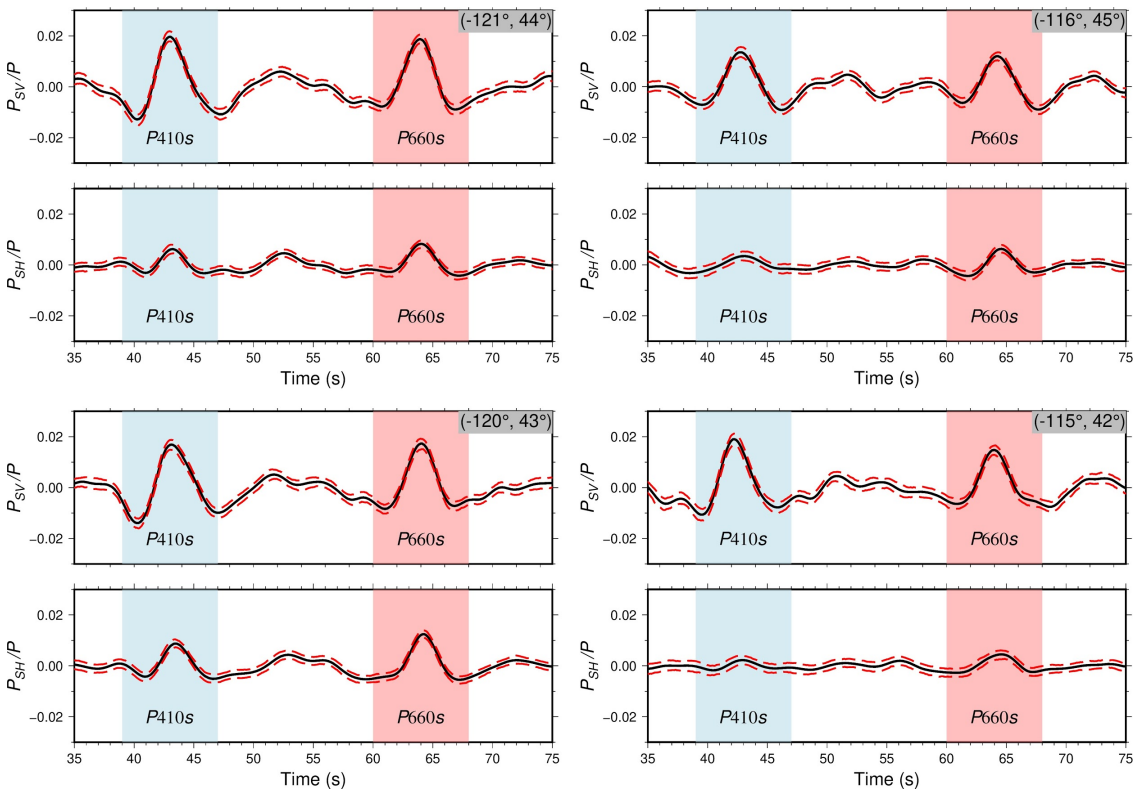

Fig. 3.S1 Additional receiver function examples that require mantle transition zone anisotropy. The locations are labeled at the top right corner. The red dashed line represents the 95% confidence level of the stacked traces from bootstrap resampling.

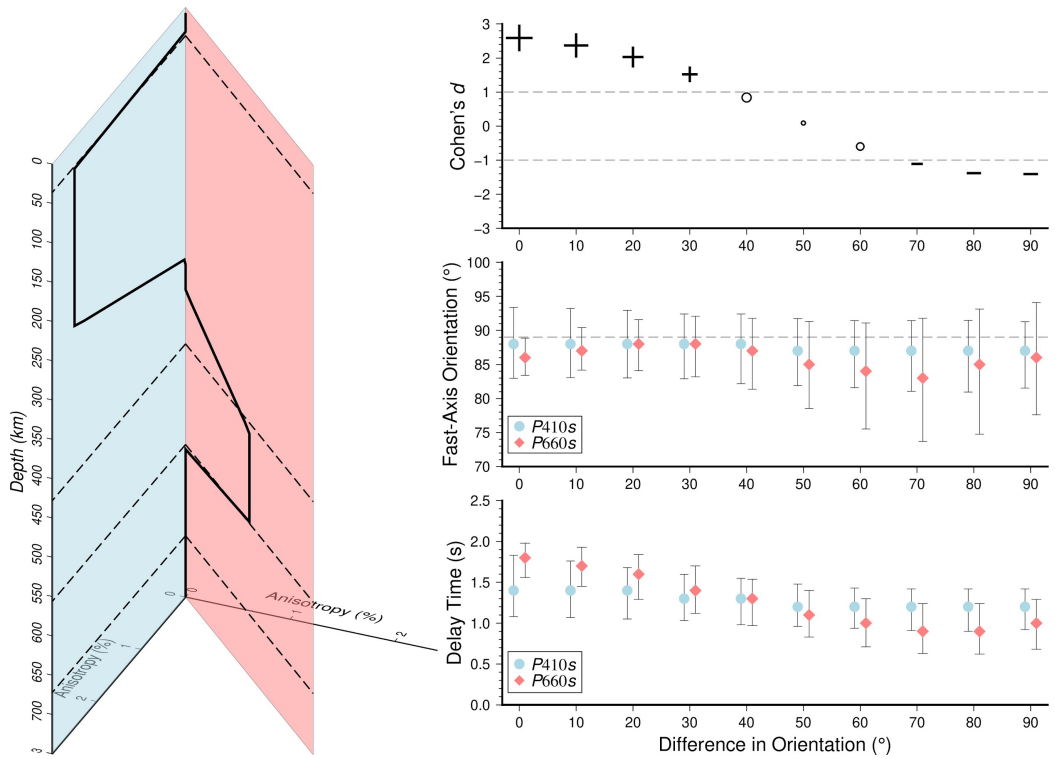

Fig. 3.S2 Synthetic results of two anisotropic layers with different orientations. Cohen's distance shows the greatest sensitivity to the variation of differential orientations among the three measurements.

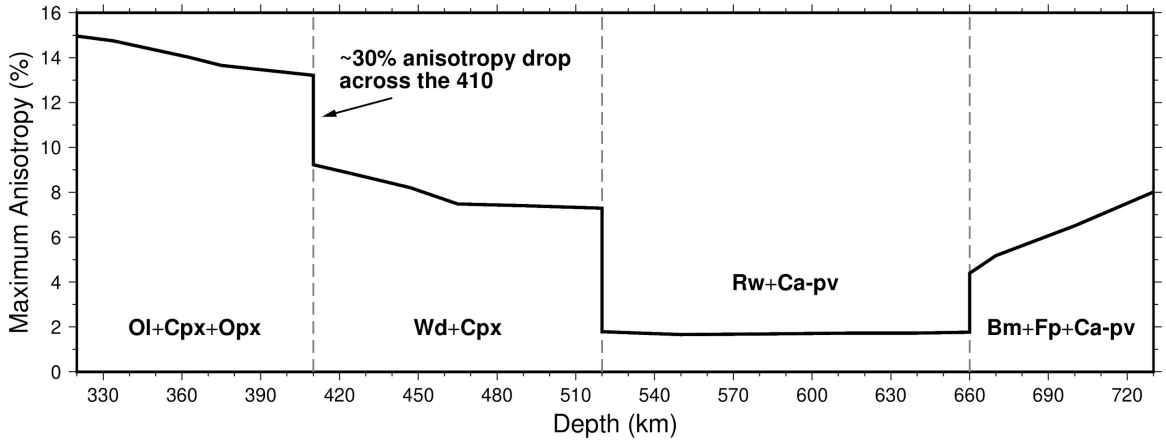

Fig. 3.S3 Maximum shear wave anisotropy indicated from a pyrolite model. There is an ~30% anisotropy drop across the 410 discontinuity primarily due to the significantly lower intrinsic anisotropy of wadsleyite compared with olivine. Only the minerals contributing to the calculated anisotropy are labeled in the figure: olivine (Ol), clinopyroxene (Cpx), orthopyroxene (Opx), wadsleyite (Wd), ringwoodite (Rw), Ca-perovskite (Ca-pv), bridgmanite (Bm), ferropericlase (Fp).

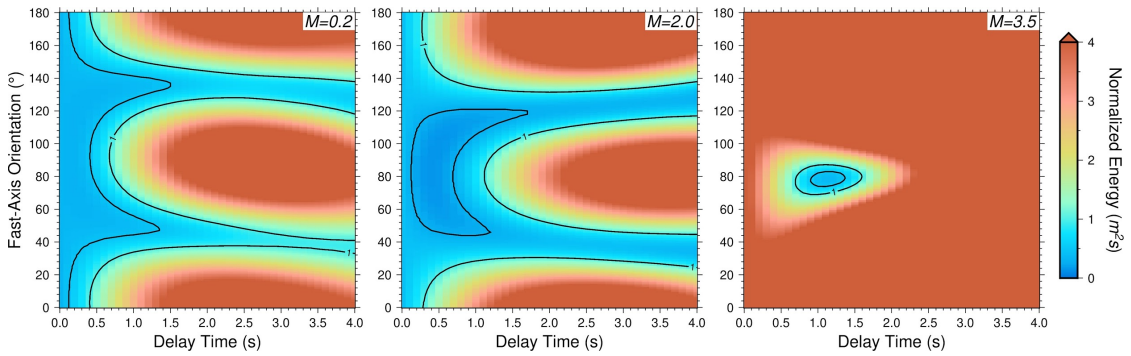

Fig. 3.S4 Examples of the energy minimization results with various *M* values. The *M* values are labeled at the top right corner. The contoured line with normalized energy equal to 1 represents the 95% confidence interval from the F-test. The inner contour represents the 68% confidence interval.

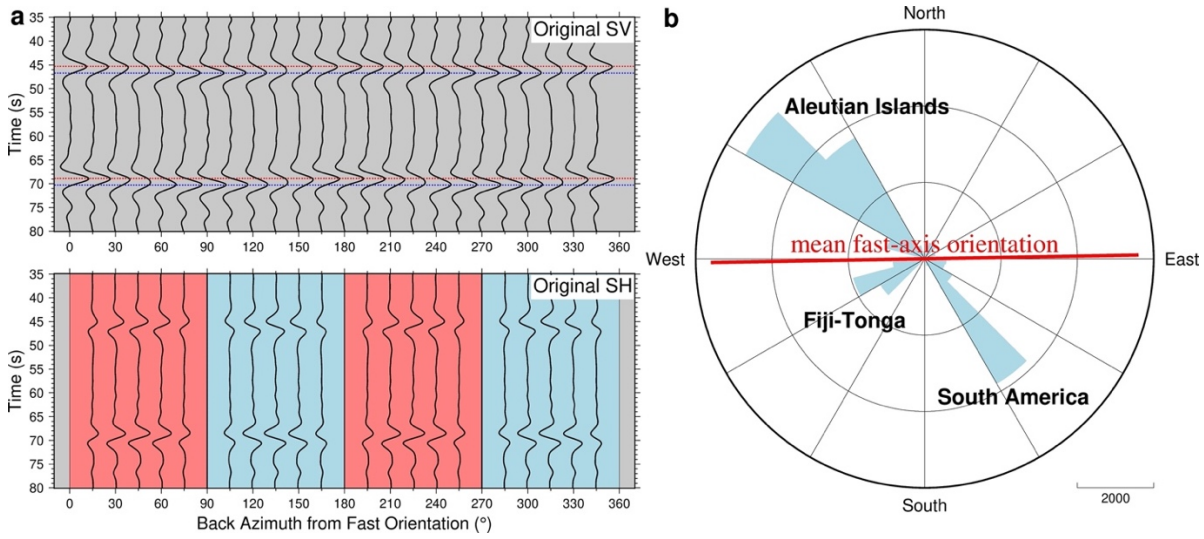

Fig. 3.S5 Synthetic receiver functions and back azimuth distribution of the PNW dataset. (a) The top panel shows synthetic receiver functions on the SV component while the bottom panel shows the SH components. The SH components flip polarity after the back-azimuth crosses the fast- or slow-axis. (b) The mean fast-axis orientation (89˚) estimated from the *P*660*s* phase is shown by the red solid line. Three regions (Aleutian Islands, South America, and Fiji-Tonga) contributed the majority of the receiver functions in this study.

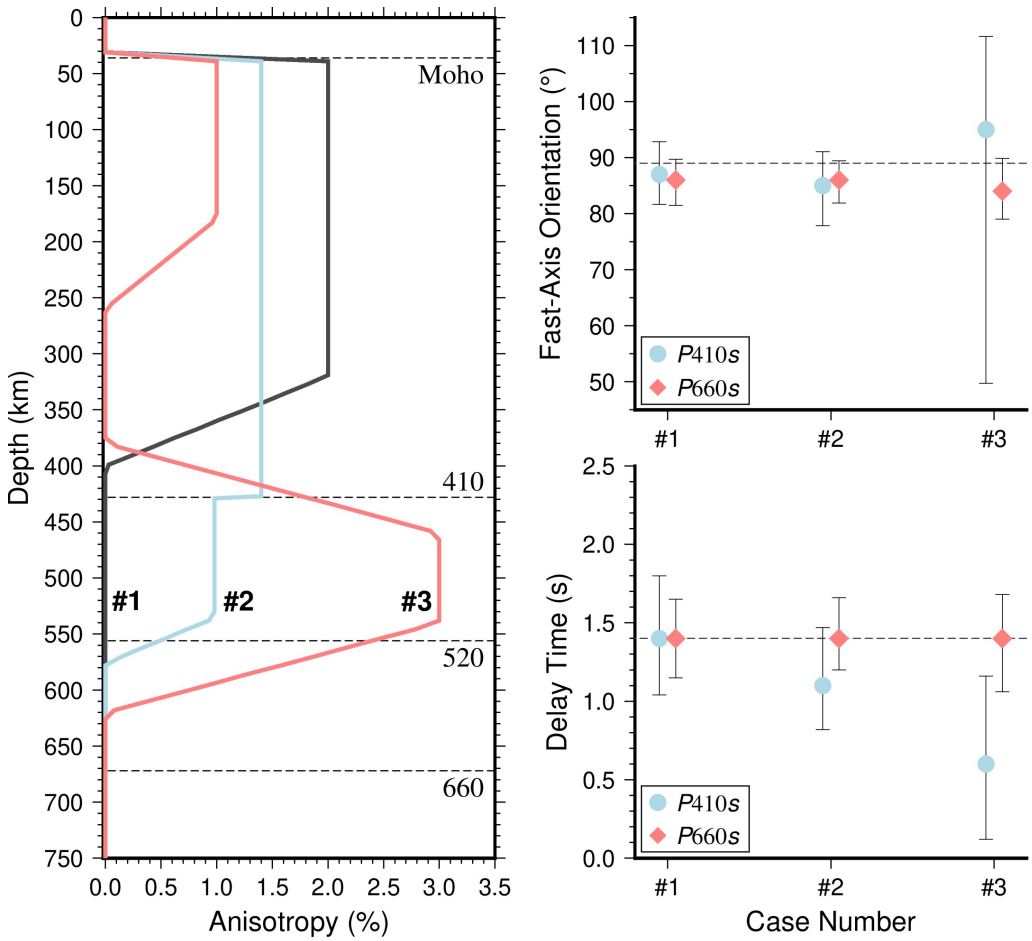

Fig. 3.S6 Forward models and splitting estimations from energy minimization method. All three input models have a fast-axis orientation of 89˚ and a delay time from *P*660*s* of ~1.4 s. The energy minimization method successfully recovers the input with the 95% confidence intervals.

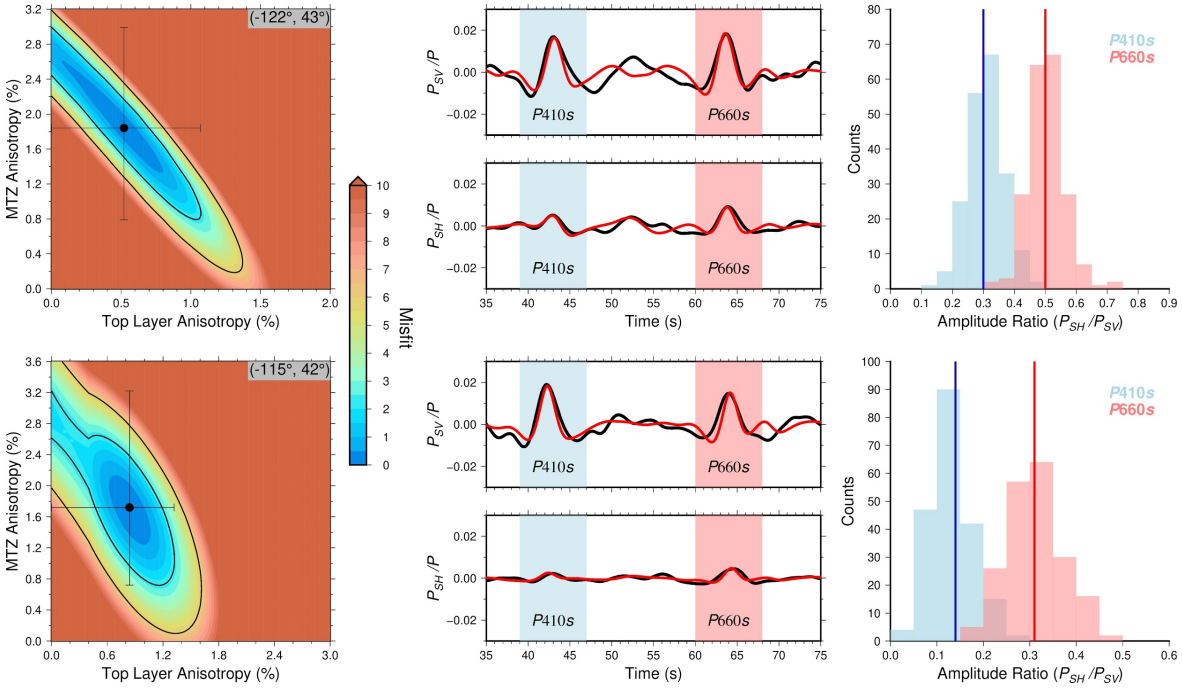

Fig. 3.S7 Examples of misfit distribution from grid search inversion and best fit model. The left panel shows the distribution of the misfit Q. The locations are labeled at the top right corner. The two black contour lines denote the 68% and 95% confidence interval of the estimated parameters respectively. We represented the intervals in Fig. 4b and c using the error bar boxing the 68% area. The middle panel gives the observed receiver functions (black) and the synthetic waveforms (red) from the best fit model. The right panel shows the observed amplitude ratio distributions and the predictions from the best fit model (vertical lines).

Network Code	DOI or Years of Operation	Network Code	DOI or Years of Operation
2G	https://doi.org/10.7914/SN/2G_2010	XC	https://doi.org/10.7914/SN/XC_1994 https://doi.org/10.7914/SN/XC_2000 https://doi.org/10.7914/SN/XC_2006
BK	https://doi.org/10.7932/BDSN	XD	https://doi.org/10.7914/SN/XD_2014
C8	2003-2017	XE	https://doi.org/10.7914/SN/XE_2005
CC	https://doi.org/10.7914/SN/CC	XH	https://doi.org/10.7914/SN/XH_1994
CN	https://doi.org/10.7914/SN/CN	XJ	https://doi.org/10.7914/SN/XJ_2000
GS	https://doi.org/10.7914/SN/GS	XK	https://doi.org/10.7914/SN/XK_2004
HW	2008-2012	XL	https://doi.org/10.7914/SN/XL_1997
IM	Permanent	XN	https://doi.org/10.7914/SN/XN_2010
IU	https://doi.org/10.7914/SN/IU	XQ	2003-2005 https://doi.org/10.7914/SN/XQ_2007
IW	https://doi.org/10.7914/SN/IW	XS	https://doi.org/10.7914/SN/XS_1999
LB	Permanent	XT	2006-2008 https://doi.org/10.7914/SN/XT_2011
LI	https://doi.org/10.7914/SN/LI	XU	https://doi.org/10.7914/SN/XU_2006
MB	https://doi.org/10.7914/SN/MB	XZ	1993-1994
NN	https://doi.org/10.7914/SN/NN	Y3	https://doi.org/10.7914/SN/Y3_2008
PN	Permanent	Y5	2006-2013
PO	2009-2012	YB	https://doi.org/10.7914/SN/YB_2005
TA	https://doi.org/10.7914/SN/TA	YC	https://doi.org/10.7914/SN/YC_2003
UO	https://doi.org/10.7914/SN/UO	YS	https://doi.org/10.7914/SN/YS_2001
US	https://doi.org/10.7914/SN/US	YW	https://doi.org/10.7914/SN/YW_2007
UU	https://doi.org/10.7914/SN/UU	YX	https://doi.org/10.7914/SN/YX_2010
UW	https://doi.org/10.7914/SN/UW	Z2	2009-2010
WY	https://doi.org/10.7914/SN/WY	ZG	https://doi.org/10.7914/SN/ZG_2006
XA	https://doi.org/10.7914/SN/XA_2008		

Table 3.S1 The network codes we used in this study and their DOIs. When DOI is not available, the operation period is given instead.

4. Revisiting the depth distribution of seismicity before and after the 2004-2008 eruption of Mount St. Helens

4.1 Introduction

Seismicity is an important indicator of changes in the magmatic system at depth beneath active volcanoes (Pesicek et al., 2018). Changes in the rate, locations, and source types can provide insight into changing conditions in the magmatic system. For example, Shapiro et al., (2017) identified earthquake clusters at two distinct depths near the Klyuchevskoy volcano group and proposed a fluid pressure transfer between the deep source and the shallow magma systems preceding volcano eruptions. Cesca et al., (2020) observed fast upward migration of the seismicity from the Moho to the surface near Comoros island and interpreted it as the drainage of a deep magma reservoir. Roman and Cashman (2018) analyzed earthquake catalogs preceding six well-monitored volcanic eruptions and proposed a top-down model for long multi-stage precursory sequences. Consequently, the reliability of these interpretations and their ability to inform future hazard forecasting heavily depends on the accuracy of earthquake detection and hypocenter estimation, especially estimates of focal depths.

Mount St. Helens (MSH) is the most active volcano in the Cascade range and has been monitored for more than four decades (Dzurisin, 2018). The permanent seismic stations operated by the Pacific Northwest Seismic Network (PNSN) and USGS Cascades Volcano Observatory routinely detect and locate local earthquakes (https://pnsn.org/). The decades-long catalog contains potential precursors to the 2004-2008 dome-building eruption and has been advancing our understanding of the evolution of the magma system from the 1980 eruption to the present (Moran et al., 2008). The catalog is widely cited to infer the depths of

magma reservoirs (e.g. Blundy et al, 2008), to identify temporal pressure changes at depths (e.g. Moran, 1994; Musumeci et al., 2002; Lehto et al., 2010; Lehto et al., 2013), and to construct regional seismic tomography models (e.g. Lee and Crosson, 1989; Waite and Moran, 2009; De Siena et al., 2014; Kiser et al., 2016; Kiser et al., 2018; Ulberg et al., 2020). To increase the reliability of their products, these studies often require empirical constraints such as a minimum azimuth gap, distance to nearest station (delta) and/or a travel time residual threshold to discard less constrained hypocenters. However, when focusing on tracking spatiotemporal changes in the magmatic system, using the catalog hypocenters may suffer from systematic bias introduced by changing network geometry and inversion processes over time. There is an apparent change in the depth distributions before and after the 2004-2008 eruption in the PNSN catalog. Given the network densification and instruments upgrades during the 2004-2008 dome-building eruption, the improved subsurface velocity profile from a densely placed temporary array in 2005 (Thelen et al., 2008), and changes in PNSN's processing system as well as location methods in 2011, a direct comparison of the catalog hypocenters may lead to misinterpreted conclusions. Instead, using a constant inversion workflow to locate the local seismicity should be preferred when inferring the spatiotemporal evolution of the magmatic system.

Temporary seismic nodes have been used to augment the spatial coverage of permanent stations at various environments and have shown great flexibility in their deployment (Glasgow et al., 2018; Wang et al., 2020). Such flexibility motivates examining the reliability of the local catalog at MSH and can separately investigate the contributions from an improved array geometry and an improved location approach. In this work, we used the data from a dense node array at MSH in the summer of 2017 to relocate catalog events

and evaluate the accuracy of their hypocenters. Motivated by the differences from the existing catalog during the month of the dense array, we then relocated events from the longer term catalog between 1997 to 2022 using PNSN phase picks that are available from the ANSS Comprehensive Earthquake Catalog (ComCat, https://earthquake.usgs.gov/data/comcat/). Cumulatively, the short-term and long-term relocation results provide new insights into the evolving depth distribution of seismicity at MSH.

4.2 Data and Method

The temporary seismic network YI contains 136 three-component nodes that recorded continuously from 2017-08-19 to 2017-09-26 (39 days, all dates in this manuscript are in UTC) at a sampling rate of 250 Hz. Based on the node locations, we divided them into four subarrays that are color coded in Figure 4.1. The sub-array on the southwest side (red) has 20 nodes. The 'new dome' array (green) has 24 nodes and was placed on the dome extruded during the 2004-2008 eruption. Its center is located ~500 m south from the CC-SEP station, which is located on the dome that grew over several years following the 1980 eruption (Lipman and Mullineaux 1981; Endo et al., 1981; Weaver et al., 1981; Swanson et al., 1983; Malone et al., 1983). The crater floor array (black) has 23 nodes and was placed near the CC-VALT station. The ring array (blue) has 69 nodes and surrounds the volcano with an average radius of ~5 km. Moreover, there are 11 permanent stations in our study area during the period and they are denoted by gray squares in Figure 4.1 and their channel information and operation period can be found in Table 4.1.

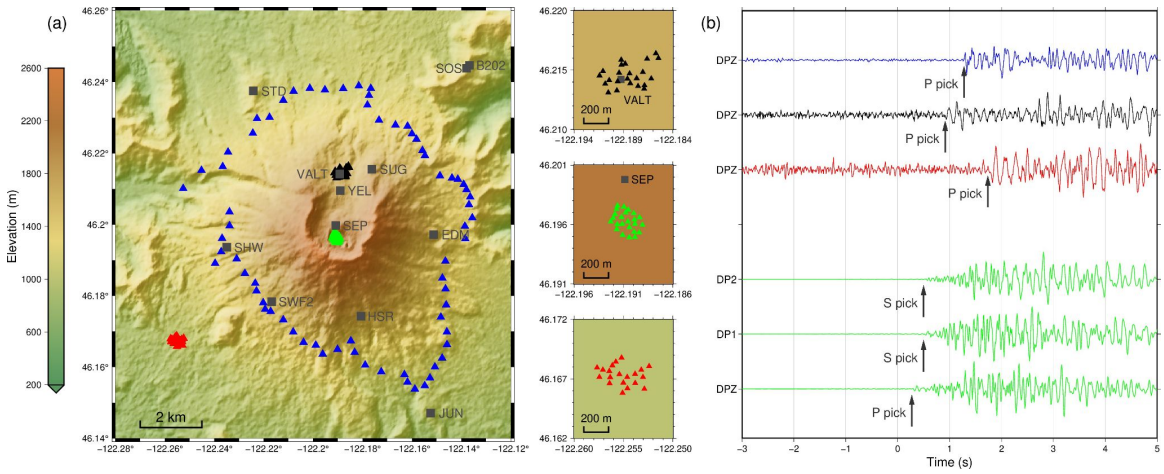

Figure 4.1 Map of seismic stations and phase pick examples. (a) The node stations are represented by colored triangles based on their locations and the side panels show detailed layout of the three densely placed sub-arrays. The permanent stations are denoted by gray squares with their names. (b) The waveform examples are color coded using the same strategy as in the station map. The node channel names are shown along the traces. The DP1 records the north-south motions, DP2 records east-west motions, and DPZ records vertical motions.

Network	Station	Operation	Channel	Network	Station	Operation	Channel
CC	SEP	2004-11-05	Z/3C*	UW	SHW	1972-10-01	Z/3C*
CC	STD	2004-10-05	3C	UW	EDM	1980-06-01	Z/3C*
CC	VALT	2006-09-30	3C	UW	HSR	1985-08-12	Z
CC	SUG	2009-08-07	Z/3C*	UW	SOS	1980-05-16	Z
CC	SWF2	2013-08-29	3C	PB	B202	2007-07-05	3C
UW	SEP	1997-09-01 to 2004-10-06	Z	UW	YEL	1981-10-01 to 2007-09-18	Z
UW	STD	1982-05-01 to 2017-09-14	Z	UW	JUN	1980-05-08 to 2019-07-12	Z

Table 4.1 Permanent stations used in this study. Note: Operation only includes the start date if the station is still working. Z in the channel column means vertical component seismometers and 3C means 3-components seismometers. Vertical component stations that were upgraded to 3C are indicated (*). The CC-SEP was upgraded to 3C on 2013-04-30. The CC-SUG was upgraded to 3C on 2014-07-29. The UW-SHW and UW-EDM were upgraded to 3C on 2021-06-18.

During the deployment period, the PNSN catalog reported 24 events within 5 km of the center of the crater (46.20˚, -122.19˚). The PNSN generated catalog is accessed through USGS's ComCat (earthquake.usgs.gov). The magnitudes range from -0.2 to 1.2. These events are typical volcano-tectonic earthquakes (Chouet and Matoza, 2013) with prominent body wave arrivals. We successfully identified 23 of the 24 catalog events from the node array and made ~1,000 phase picks (see examples from Figure 4.1). We were able to pick S onsets for 15 events and most of them came from the dome array and SEP. For comparison, the events have 5.8 P picks and 2.5 S picks on average for their PNSN hypocenters. Adding the node array boosts the number of P and S picks to 41.9 and 3.6 per event, respectively. We assigned a uniform weight (1.0) for all the picks from the permanent stations and the ring array. The southwest, dome and floor arrays were each assigned a summed weight of 2.0 for their P picks if there are more than 2 phase picks. If there is only one phase pick from the arrays, the weight is 1.0. The same weighting was used for S picks. This makes the contributions from the three dense sub-arrays twice as important as a single station but avoids overweighting them since they are too closely spaced to be considered completely independent observations.

When extending the relocated catalog to between 1997 and 2022, we avoided the time of the 2004-2008 eruption to focus on background seismicity and used the phase picks from PNSN to maintain a common set of input data. Our analysis starts in 1997 because the dome station SEP was installed in that year. The 2004-2008 eruption was avoided because of the extreme rate of seismicity and the likelihood that abundant shallow seismicity and tremor diminished the ability to detect deeper events (Moran et al, 2008). The network evolved over the study period, mostly by the addition of new stations and upgrades from a vertical

component to 3-component seismographs (Table 4.1). The only exception in our study region is the station YEL which was removed in 2007-09-18 and replaced by VALT. The two stations are a few hundred meters apart and therefore provide similar constraints to earthquake hypocenter estimates. Thus, we included the station during the relocation for events before its retirement. We requested PNSN phase picks and their associated weights from events with epicenters within 5 km from the crater's center. We discarded events with less than 4 phase picks since we cannot reliably locate them. The choices mentioned above result in 7321 toal events for relocation between 1997-01-01 and 2022-03-01.

To estimate hypocenters of the local events, we used the fast marching method (Rawlinson and Sambridge, 2004) for 3D wavefront tracking to trace P and S rays from each station (Figure 4.2). We adopted the 3D P-wave velocity model from Kiser et al., (2016) and generated an S-wave velocity by scaling the P-wave model using the empirical relationships from Brocher (2005). Topography effects were accounted for by filling the air layer grids with a velocity of 0.34 km/s. The air layer was defined as grids above the surface topography from a 30 m digital elevation model (USGS, 2017). The 0.34 km/s represents the speed of sound in air at 20 °C and 1 atm. The grid interval along both latitude and longitude directions is 0.001 degrees and that along the depth dimension is 0.1 km. We then calculated the hypocenters by minimizing a weighted L2 misfit between the predicted and measured arrival times (see an example in Figure 4.2). Minimizing an L2 misfit will automatically require the event origin time to be the weighted average of origin time estimates from all stations. Consequently, the absolute location algorithm only searches in three dimensions.

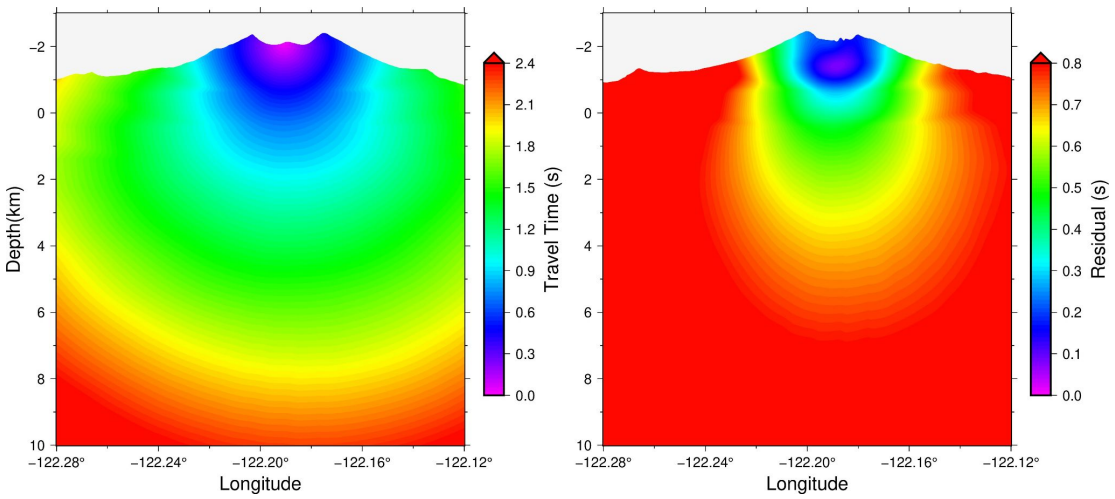

Figure 4.2 P wave travel time field from station SEP (left) and a residual time example from event 2017-08-24T05:16:36 (right).

4.3 Results

When relocating the 23 PNSN events that occurred during the 2017 nodal deployment, the resulting hypocenters concentrate beneath the crater at depths between sea level and 1 km above it (Figure 4.3a and 4.3b). The mean hypocenter movement from catalog locations is 2.86 km with an averaged depth movement of 2.53 km upward. Locating the events with only the P picks from all stations gives similar hypocenter results (Figure 4.S1), suggesting that our results are not highly dependent on interpretations of S-wave onsets.

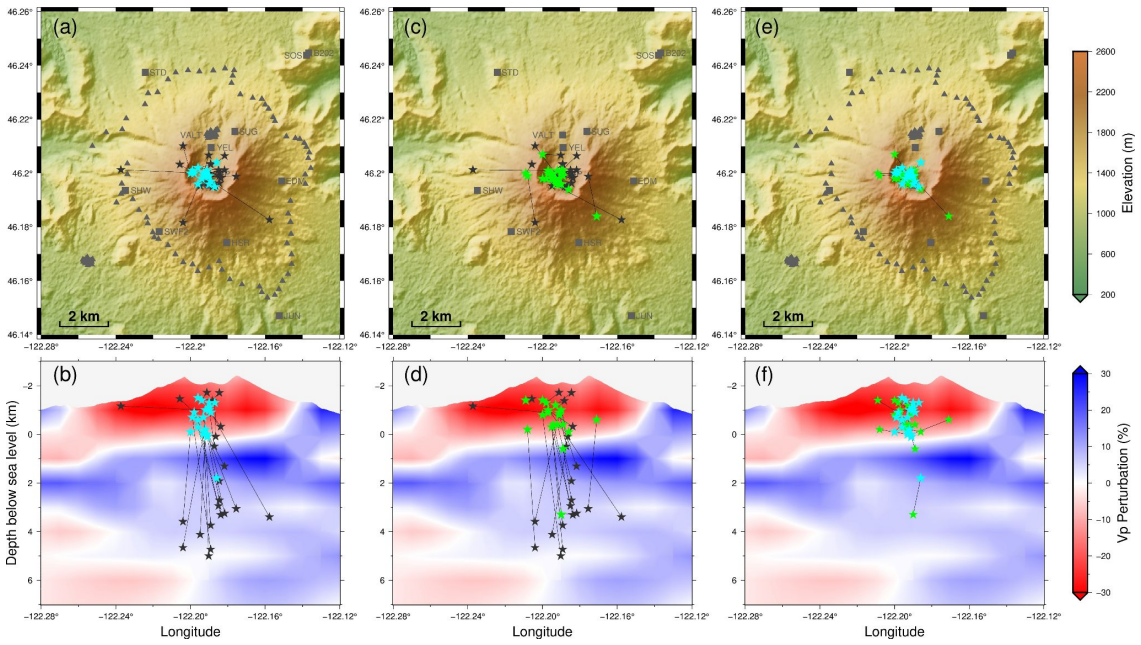

Figure 4.3 Comparison of three approaches to locate seismicity during the node array. The preferred earthquake hypocenters using all phase picks from the node and PNSN arrays (cyan stars), using only PNSN picks with the hypocenter estimation method from this study (green stars), and the PNSN catalog locations (black stars) are shown. The cross-sections in (b, d, f) are sliced along a latitude of 46.20˚. The Vp perturbations are taken from the tomography model of Kiser et al., (2016). (a, b) Comparison between the preferred hypocenters when using all available picks (cyan) and the PNSN catalog locations (black). (c, d) Comparison between hypocenters estimated using PNSN picks with the estimation method from this study (green) and their PNSN catalog locations (black). (e, f) Comparison between the preferred hypocenters when using all picks (cyan) with those estimated using only PNSN picks (green) but with the same hypocenter estimation method from this study.

Node waveform examples from three different depths provide further indications that most seismicity is shallow and centrally located beneath the dome array. We show the waveforms from example events with depths of 1.8 km, 0 km, and -1.4 km below sea level, respectively (Figure 4.4). The traces are color-coded to match their locations in Figure 4.1 and are sorted by azimuth within each sub-arrays. We see that only the deep event clearly excites signals on the southwest array, which is farther from the dome (Figure 4.4a). In contrast, the sea level event lacks clear expression on the southwest array (Figure 4.4b). The

shallowest event only generates clear signals at the dome stations and some ring stations, which have long coda on their horizontal components possibly due to reverberation within the edifice (Neuberg and Pointer, 2000). Moreover, the arrival times at the ring stations become later than those from the dome array for the shallowest event (Figure 4.4c), which is consistent with a shallow origin.

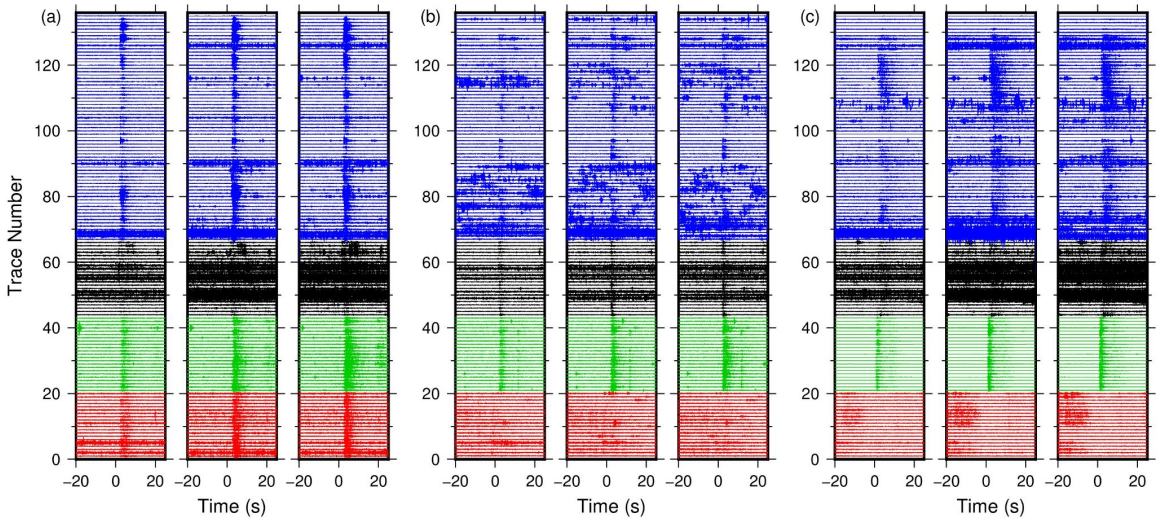

Figure 4.4 Waveform examples from events with three different depths. The waveforms are color-coded to match the station locations in Figure 1. (a) event depth of 1.8 km below sea level. The three columns show the DPZ (vertical), DP1 (north-south), and DP2 (east-west) channels from the left to right respectively. (b) same as (a) but for an event depth at sea level (0.0 km). (c) same as (a) but for an event depth of 1.4 km above sea level (-1.4 km).

To separate the effects of adding the dense node array from the effects of the hypocenter estimation approach, the hypocenters for the same events were also estimated using only the PNSN array but with the hypocenter estimation approach from this study using a 3D velocity model (Figure 4.3, c and d). The relocated hypocenters are also more concentrated beneath the crater. When comparing the two sets of relocated hypocenters, we see minor improvements from adding the node array picks in addition to the PNSN picks

(Figure 4.3, e and f). A tighter horizontal clustering of seismicity beneath the dome complex in the summit crater is shown with the dense node array. The mean hypocenter movement is 0.73 km with an average depth movement of 0.37 km. These movements are much smaller than those from the PNSN locations to our preferred results, which are 2.86 km for hypocenter and 2.53 km for depth. The comparison suggests that the 3D velocity model and the ray tracing algorithm play more important roles in updating the hypocenters. Assuming the 3D velocity models can be used for locating earlier seismicity at MSH, our finding motivates relocation of the longer term catalog to check for potential systematic bias.

We extended the relocated catalog to local events at MSH from 1997 to 2022 (Figure 4.5). We excluded the events during the 2004-2008 dome-building eruption due to our focus on background seismicity at MSH. After discarding events with a relocated epicenter more than 5 km from MSH, the preferred earthquake depths form a continuous band of seismicity between sea level and ~1 km above it (Figure 4.5, see Figure 4.S2 for a version without event depths from PNSN). For the cumulative study period, about 66% (4866 out of 7321) of the relocated events move to a shallower depth with an average upward movement of 1.68 km. Focusing on the post-2008 events, about 86% move to a shallower depth with an average upward movement of 2.16 km. The concentration of seismicity between sea level and ~1 km above it still exists even if we locate the post-2008 events only using the stations available before 2004 (Figure 4.S3), suggesting that array geometry plays a minor role in the depth estimates (Steve and Schmandt, 2015).

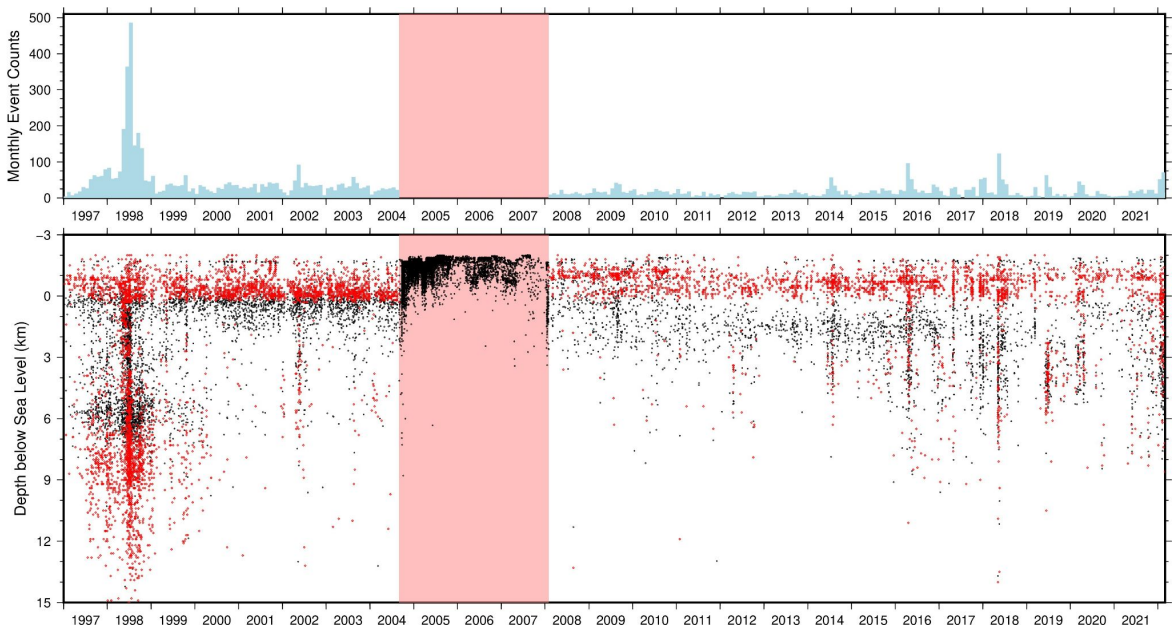

Figure 4.5 Seismicity rate and depth distribution beneath MSH from 1997-2022. Monthly event count is shown for events within 5 km of MSH, with depths from our relocated catalog (red) and the PNSN catalog (black). The 2004-2008 dome-building eruption period is covered by the pink box and earthquakes from that period were not relocated.

4.4 Discussion

The most prominent result of the earthquake relocation analysis is that the depth distribution of seismicity at MSH post-2008 is more similar to the depth distribution prior to the 2004-2008 dome-building eruption (Figure 4.6). The PNSN catalog shows a concentration of seismicity between -1 to 0 km below sea level prior to 2004 but that is replaced by deeper and more diffuse events between 0 to 3 km below sea level following the 2004-2008 eruption, apparently indicating a change in seismogenic structures within the MSH magmatic system. The distinct depth distributions were taken as evidence of a slower pressurization rate of the shallow conduits beneath MSH after the 2004-2008 dome-building eruption (Dzurisin, 2018). However, the relocated catalog eliminates the basis for such an interpretation of change in the magmatic system (Figure 4.6). The relocated results using a

consistent velocity model and processing approach for the entire study period show that concentrated seismicity at -1 to 0 km below sea level persists before and after the 2004-2008 dome-building (Figure 4.6). Subtle pre- and post-eruption changes are observed in the relocated catalog, such as a greater concentration of events near -1.5 km below sea level from 2008-2010, which suggests a slight shallowing of seismicity rather than a deepening in previous results (Figure 4.5). However, the dramatic change between the pre- and post-eruption depth distribution in the PNSN catalog becomes much more subdued in the relocated catalog (Figure 4.6). The main change that remains in the relocated catalog is that the number of events at depths greater than 5 km below sea level is greater prior to 2004, which mostly results from an elevated rate of deeper seismicity and inferred magmatic recharge centered in 1998 (Musumeci et al., 2002; Figure 4.5).

Since the PNSN catalog and our new long-term relocation results used the same phase picks, the difference is most likely due to the difference in locating methods. The location algorithm used by PNSN traces P and S rays in a 1D velocity model and introduces empirical station corrections to account for 3D velocity anomalies and site topography. Consequently, inconsistent empirical corrections from different stations could lead to systematic location bias that can change each time a station is added or removed. Several stations were added or upgraded during the 2004-2008 eruption, thereby providing one potential source of bias when comparing pre-2004 and post-2008 hypocenters. Alternatively, the difference in the location solver could introduce bias in the results. In 2011, PNSN switched from SPONG, an adaption of FASTHYPO (Herrmann, 1979) to Hypoinverse (Klein, 1985). Subtle differences in inversion techniques between the two methods can lead to differences in locations, where a local minima may be preferred erroneously. This

behavior has been recognized anecdotally for some events at Mount St. Helens, though never published. In contrast, here we fixed the 3D velocity model, location method and ray tracing method for both periods, making the relocated hypocenters more comparable. Additionally, we tested the effects of using only the stations available before 2004 and found a similar event depth distribution (Figure 4.S3). Therefore, we suggest that the relocated time-depth results better represent the distribution of seismicity beneath MSH before and after the 2004-2008 eruption.

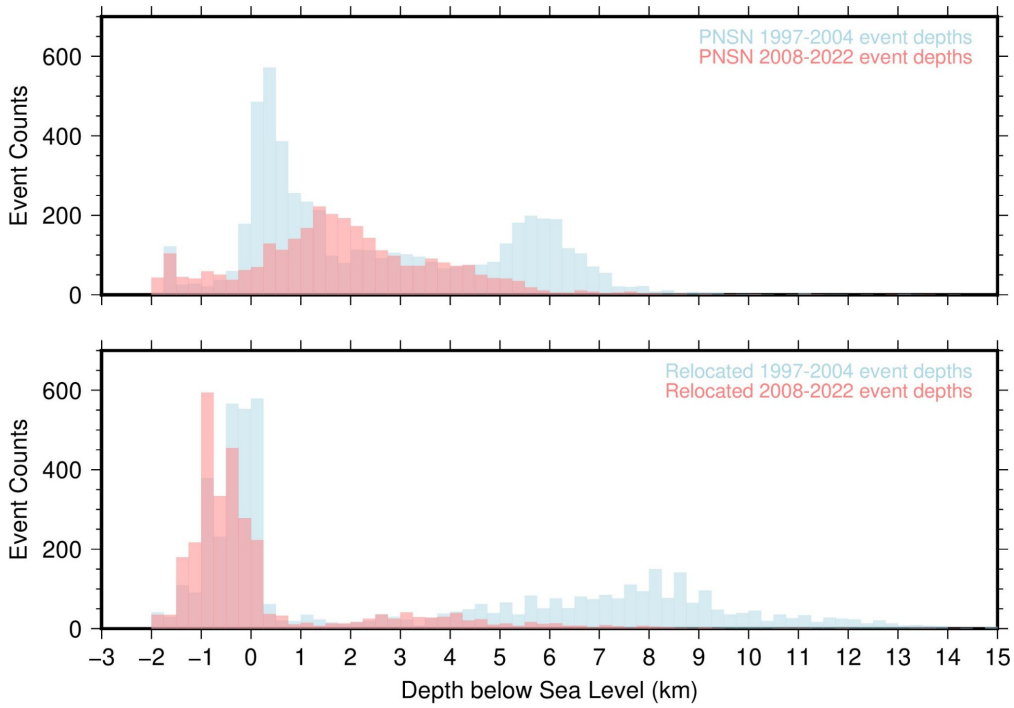

Figure 4.6 Estimates of the depth distribution of MSH seismicity. The depth distribution of pre-2004 (blue) and post-2008 (red) local events at MSH from the PNSN catalog (top) and from the relocated catalog (bottom).

Most of the relocated event depths are between sea level and ~1 km above it (Figure 4.6), which is significantly shallower than petrologic studies suggest for the localized sources of magma that fed the 2004-2008 dome-building eruption (~3 km beneath sea level from

Pallister et al., 2008). The concentration of shallow seismicity is also shallower than the estimated depths of the primary upper crust magma chamber at MSH: ~5-11 km below sea level from Blundy et al., (2008); 3.5-14 km below sea level from Kiser et al., (2018); 3-12 km beneath surface from Hill et al., (2009); and a top depth of 3-8 km beneath surface from Anderson and Segall, (2013). Consequently, the isolated shallow peak in seismicity may represent stress rebalance in conduits above magma storage depths, perhaps as a result of magmatic volatiles migrating through fractures rather than their previous interpretation as inputs to the silicate melt reservoirs at greater depths (Lehto et al., 2013). Moran et al., (2008) proposed that the concentration of shallow seismicity before 2004 could represent a fracture zone near the base of a solid plug which extends from the surface down to sea level. If so, the continuity of shallow seismicity after the 2004-2008 eruption suggests relatively quick formation of a solid plug creating conditions similar to those of the pre-2004 period. Indeed, seismicity right at the end of the 2004-2008 eruption extended to 3 km below sea level for the first time since before the 2004 eruption (Dzurisin et al., 2015). The earthquake frequency from 2008 to 2013 (3.1 events/week) is less than half of that from 1999 to 2004 (7.0 events/week) (Figure 4.5). Assuming the earthquake detection threshold is the same for the two periods, a smaller seismicity rate could represent a relatively weak solid plug or less intense pressure influx of magmatic volatiles from below.

The relocated time-depth catalog shows a strong correlation between earthquake count peaks and deep seismicity clusters (Figure 4.5). The monthly count peaks in the years of 2002, 2014, 2016, 2018, and 2019 all associate with increases in volcano-tectonic seismicity ~1-10 km below sea level. To explore the temporal relationships between the shallow and deep seismicity near these peaks in detail, we calculated their cumulative event

count within a five month time window (Figure 4.7). The depth to split shallow and deep events is set at 0.5 km below sea level, as suggested by the event distribution in Figure 4.6. The detailed view suggests various temporal patterns between earthquakes at different depths (Figure 4.7). Near the 2002, 2014, and 2018 peaks, both the shallow and the deep seismicity show sharp increases at similar times. However, near the 2016 peak, the shallow seismicity rate increases ~2 weeks before deeper seismicity. Near the 2019 peak, the shallow seismicity appears decoupled from the deeper earthquakes. Moreover, if we look at the shallow seismicity rate before and after clustered deep earthquakes, the 2018 peak also differs from the 2014 one. Near the 2014 peak, the elevated shallow seismicity rate decays weeks after cessation of the deeper earthquakes. In contrast, near the 2018 peak, the shallow seismicity rate stays high after the cessation of deeper earthquakes. These results suggest a complex fluid-pressure exchange system beneath MSH, in which some sequences of elevated seismicity reflect tightly coupled changes between shallower and deeper parts of the magmatic system while others involve substantial lag times.

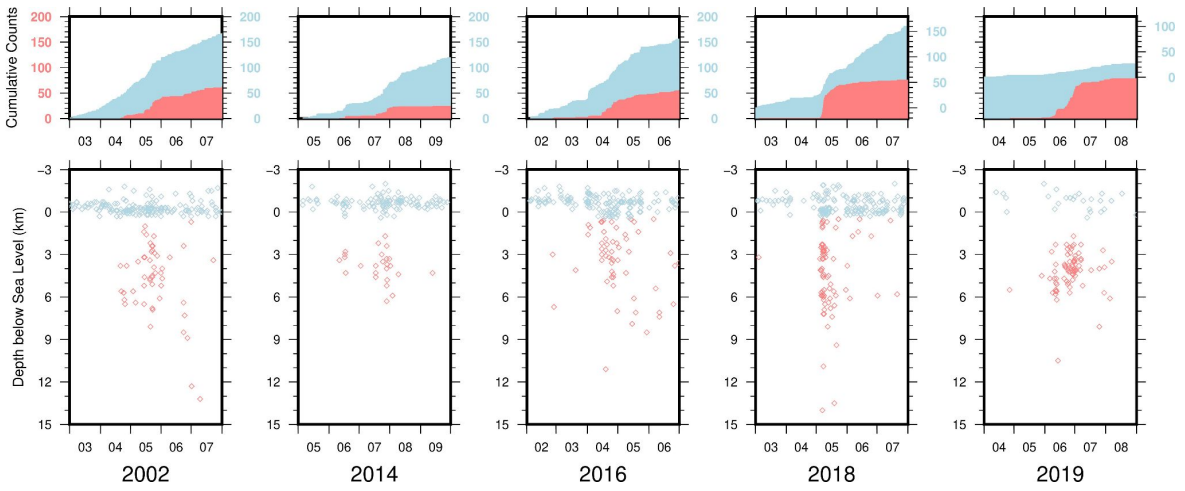

Figure 4.7 Comparison of shallower and deeper activity during episodes of elevated seismicity. (Top) The cumulative event counts of shallow (blue; less than 0.5 km below sea level) and deep (red; greater than 0.5 km below sea level) earthquakes during a five-months window. A flat line means no earthquakes and increases in slope represents increases of seismicity rate. Note that the deep events (red, left side) share a vertical axis but the vertical axis of shallow earthquakes (blue, right side) counts in 2018 and 2019 are different from the other 3 panels. (Bottom) The time-depth distribution of the seismicity. The horizontal axis marks the year and the months.

In addition to the concentration of shallow seismicity, our relocated earthquakes reveal a southward trend with increasing depth of the deep earthquakes (Fig. 4.8). In the PNSN catalog, the local seismicity is centered beneath the crater and their maximum depth is about 10 km. The hypocenters show little variations with increasing depth (Fig. 4.8a&4.8b). In contrast, the relocated earthquake depths are more diffuse in depth and their hypocenters show a clear trend towards south when the earthquake depth increases (Fig. 4.8c). According to Figure 4.5, most of the deep earthquakes are from the 1998 deep cluster, which was interpreted as a period of magma recharge (Musumeci et al., 2002). Therefore, our relocated hypocenters suggest the recharges may start from a deeper southern source region and the distribution of the deep earthquakes could indicate the pathway of magma migration. It is noteworthy that the absolute location method we used in this study suffers from a tradeoff

between small hypocenter offsets and velocity perturbation along the paths. Therefore, the distribution of the hypocenters may not represent the geometry of the magma system well. To improve the resolution, a detailed investigation on their relative locations is needed (Musumeci et al., 2002).

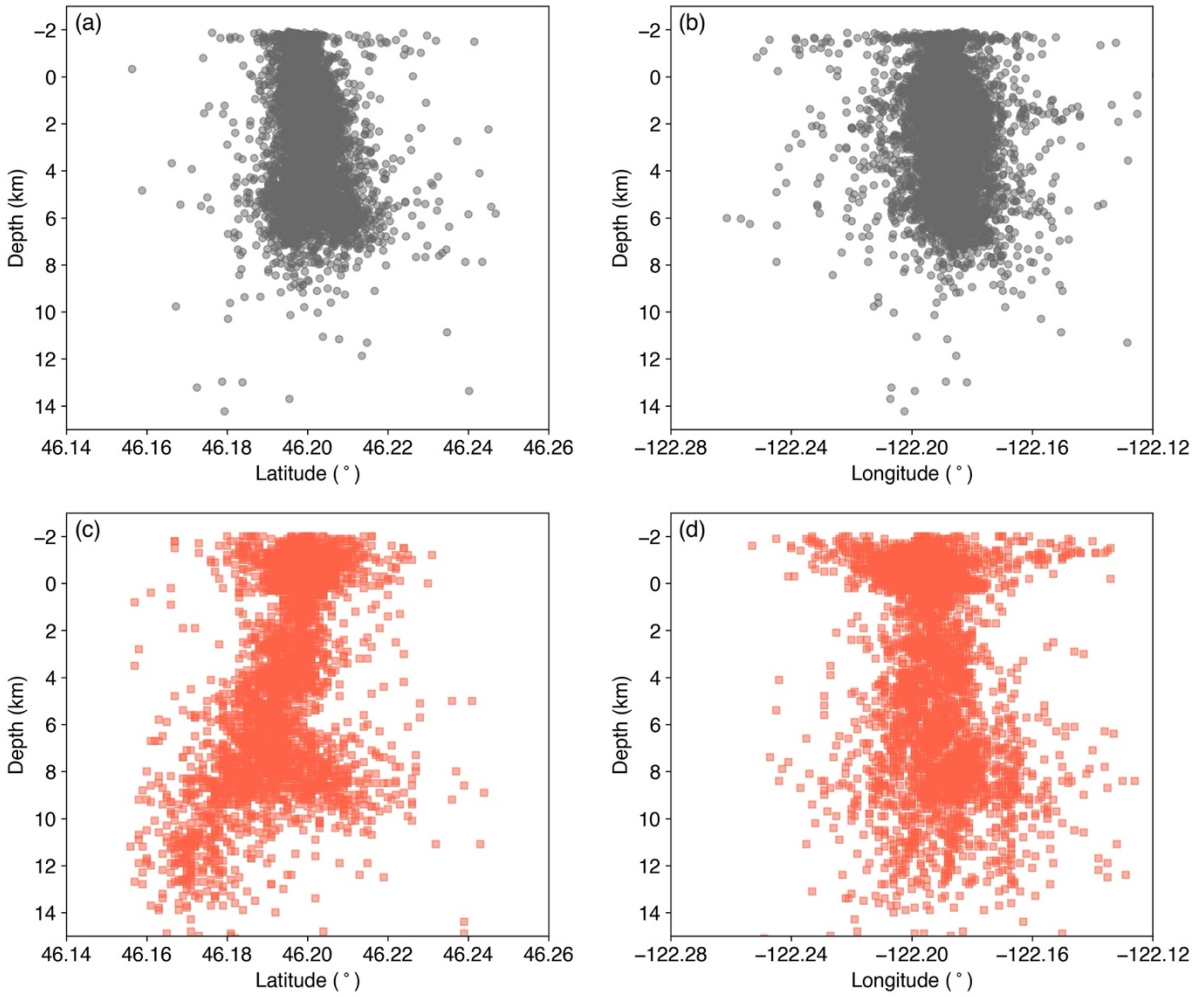

Fig. 4.8. 3D distribution of local earthquakes near MSH. (a&b) Projected PNSN earthquake locations in north-south direction and in east-west direction. (c&d) Projected relocated earthquake locations north-south direction and in east-west direction.

4.5 Conclusions

We relocated 23 earthquakes near MSH in 2017 with a dense array of three-component nodal seismometers and found most of the events moved to shallower depths and were more centrally focused beneath the crater. The average hypocenter movement from the PNSN catalog locations to our relocated hypocenters is 2.86 km, which is sufficiently large to confound interpretations of change in the magmatic system at depth. After comparing the hypocenter estimates from all available phase picks and from catalog phase picks, we found that most of the hypocenter movement resulted from the location method (including the input velocity model), with more minor effects due to the change in the number and spatial distribution of seismometers. The relocated hypocenters motivated longer term examination of changes in the depth distribution of MSH seismicity. We then relocated the PNSN catalog events from 1997 to 2022 (excluding the 2004-2008 dome-building eruption) using the same phase picks but with the updated velocity model and 3D travel time calculation method applied to the node array in 2017. The relocated hypocenters show a continuously active concentration of seismicity between sea level and ~1 km above it, suggesting similar magmatic conditions before and after the 2004-2008 dome-build eruption. Importantly, this result contrasts with the apparent change in depth between the pre- and post-eruption seismicity in the PNSN catalog. Changes in the hypocenter estimation workflow rather than changes in the magmatic system are likely to be the origin of the apparent change in seismicity depth distribution. Thus, the relocation results highlight the importance of testing the effects of any processing changes when maintaining long-term seismicity catalogs and they indicate that the dome-building eruption did not cause a major long-lived reorganization of seismogenic structures near the top of the magmatic system.

Correlations between seismicity in the shallow cluster just above sea level and at greater depths below sea level suggest transient changes in fluid-pressure exchange between shallow conduits and deeper magma reservoirs during periods of elevated seismicity. However, the catalog shows variable time lags between changes in the rate of shallower and deeper seismicity. Thus, it is unclear if these episodes of elevated seismicity are consistently initiated by either top-down or bottom-up processes.

4.6 Supplementary

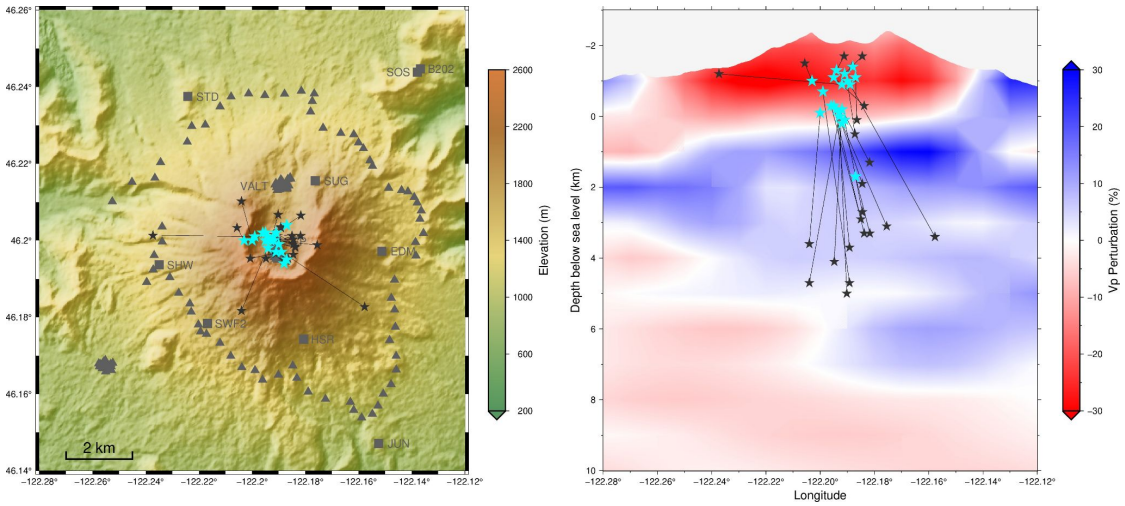

Figure 4.S1 Comparison between the preferred earthquake hypocenters using only P phase picks (cyan stars) and their PNSN catalog locations (black stars). The cross section is sliced along a latitude of 46.20˚. The Vp perturbation is taken from the tomography model of Kiser et al., (2016).

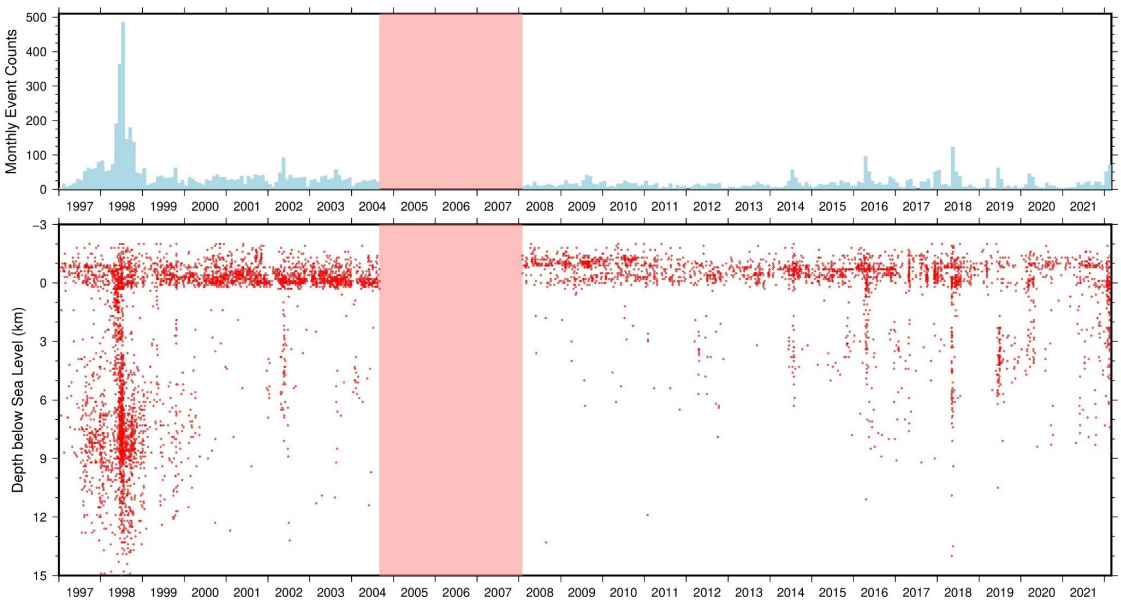

Figure 4.S2 Monthly events count within 5 km from MSH and their depths from the relocated catalog (red diamonds). The 2004-2008 dome-building eruption period is covered by the pink box and earthquakes from the period were excluded during the relocation.

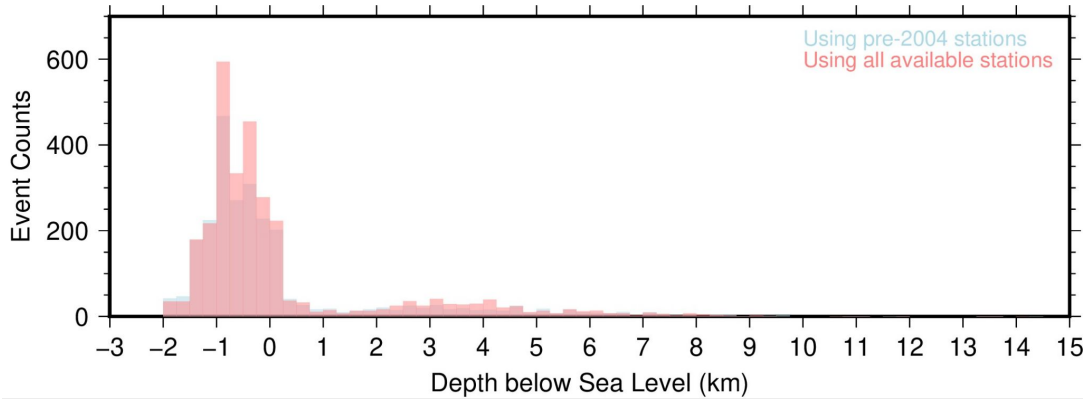

Figure 4.S3 Relocated depths distributions of post-2008 events using just pre-2004 stations (blue) and using all stations (red). We discarded events with less than 4 phase picks so using fewer stations also ended up with fewer earthquakes.

References

- Alisic, L., Gurnis, M., Stadler, G., Burstedde, C., & Ghattas, O. (2012). Multi-scale dynamics and rheology of mantle flow with plates. Journal of Geophysical Research: Solid Earth, 117(B10).
- Anderson, D. L., & Bass, J. D. (1986). Transition region of the Earth's upper mantle. Nature, 320(6060), 321-328.
- Anderson, K., & Segall, P. (2013). Bayesian inversion of data from effusive volcanic eruptions using physics-based models: Application to Mount St. Helens 2004–2008. Journal of Geophysical Research: Solid Earth, 118(5), 2017-2037.
- Ballmer, M. D., Schmerr, N. C., Nakagawa, T., & Ritsema, J. (2015). Compositional mantle layering revealed by slab stagnation at~ 1000-km depth. Science advances, 1(11), e1500815.
- Becker, T. W., Lebedev, S., & Long, M. D. (2012). On the relationship between azimuthal anisotropy from shear wave splitting and surface wave tomography. Journal of Geophysical Research: Solid Earth, 117(B1).
- Bissig, F., Khan, A., Tauzin, B., Sossi, P. A., Munch, F. D., & Giardini, D. (2020). Multi-Frequency Inversion of Ps and Sp Receiver Functions: Methodology and Application to USArray Data. Journal of Geophysical Research: Solid Earth, e2020JB020350.
- Blundy, J., Cashman, K. V., Berlo, K., Sherrod, D. R., Scott, W. E., & Stauffer, P. H. (2008). Evolving magma storage conditions beneath Mount St. Helens inferred from chemical variations in melt inclusions from the 1980–1986 and current (2004–2006) eruptions. A volcano rekindled: the renewed eruption of Mount St. Helens, 2006, 755-790.
- Bodin, T., Sambridge, M., Tkalčić, H., Arroucau, P., Gallagher, K., & Rawlinson, N. (2012). Transdimensional inversion of receiver functions and surface wave dispersion. Journal of Geophysical Research: Solid Earth, 117(B2).
- Brocher, T. M. (2005). Empirical relations between elastic wavespeeds and density in the Earth's crust. Bulletin of the seismological Society of America, 95(6), 2081-2092.
- Cesca, S., Letort, J., Razafindrakoto, H. N., Heimann, S., Rivalta, E., Isken, M. P., ... & Dahm, T. (2020). Drainage of a deep magma reservoir near Mayotte inferred from seismicity and deformation. Nature Geoscience, 13(1), 87-93.
- Chevrot, S. (2000). Multichannel analysis of shear wave splitting. Journal of Geophysical Research: Solid Earth, 105(B9), 21579-21590.
- Chouet, B. A., & Matoza, R. S. (2013). A multi-decadal view of seismic methods for detecting precursors of magma movement and eruption. Journal of Volcanology and Geothermal Research, 252, 108-175.
- De Siena, L., Thomas, C., Waite, G. P., Moran, S. C., & Klemme, S. (2014). Attenuation and scattering tomography of the deep plumbing system of Mount St. Helens. Journal of Geophysical Research: Solid Earth, 119(11), 8223-8238.
- Deuss, A., & Woodhouse, J. (2001). Seismic observations of splitting of the mid-transition zone discontinuity in Earth's mantle. Science, 294(5541), 354-357.

- Deuss, A., Redfern, S. A., Chambers, K., & Woodhouse, J. H. (2006). The nature of the 660-kilometer discontinuity in Earth's mantle from global seismic observations of PP precursors. Science, 311(5758), 198-201.
- Dziewonski, A. M., & Anderson, D. L. (1981). Preliminary reference Earth model. Physics of the earth and planetary interiors, 25(4), 297-356.
- Dzurisin, D. (2018). Mount St. Helens retrospective: Lessons learned since 1980 and remaining challenges. Frontiers in Earth Science, 6, 142.
- Dzurisin, D., Moran, S. C., Lisowski, M., Schilling, S. P., Anderson, K. R., & Werner, C. (2015). The 2004–2008 dome-building eruption at Mount St. Helens, Washington: epilogue. Bulletin of Volcanology, 77(10), 1-17.
- Endo, E. T., Malone, S. D., Noson, L. L., & Weaver, C. S. (1981). Locations, magnitudes, and statistics of the March 20–May 18 earthquake sequence. US Geol. Surv. Prof. Pap, 1250, 93-107.
- Fischer, K. M., & Wiens, D. A. (1996). The depth distribution of mantle anisotropy beneath the Tonga subduction zone. Earth and Planetary Science Letters, 142(1-2), 253-260.
- Frost, D. J. (2008). The upper mantle and transition zone. Elements, 4(3), 171-176.
- Girard, J., Amulele, G., Farla, R., Mohiuddin, A., & Karato, S. I. (2016). Shear deformation of bridgmanite and magnesiowüstite aggregates at lower mantle conditions. Science, 351(6269), 144-147.
- Glasgow, M. E., Schmandt, B., & Hansen, S. M. (2018). Upper crustal low-frequency seismicity at Mount St. Helens detected with a dense geophone array. Journal of Volcanology and Geothermal Research, 358, 329-341.
- Green, D. H., & Falloon, T. J. (1998). Pyrolite: a Ringwood concept and its current expression. The Earth’s mantle: composition, structure, and evolution, 311-380.
- Hansen, S. M., & Schmandt, B. (2015). Automated detection and location of microseismicity at Mount St. Helens with a large-N geophone array. Geophysical Research Letters, 42(18), 7390-7397.
- Hao, S., Wang, W., Qian, W., & Wu, Z. (2019). Elasticity of akimotoite under the mantle conditions: Implications for multiple discontinuities and seismic anisotropies at the depth of~ 600–750 km in subduction zones. Earth and Planetary Science Letters, 528, 115830.
- Hawley, W. B., & Allen, R. M. (2019). The fragmented death of the Farallon plate. Geophysical Research Letters, 46(13), 7386-7394.
- Herrmann, R. B. (1979). FASTHYPO—a hypocenter location program. Earthquake notes, 50(2), 25-38.
- Hill, G. J., Caldwell, T. G., Heise, W., Chertkoff, D. G., Bibby, H. M., Burgess, M. K., ... & Cas, R. A. (2009). Distribution of melt beneath Mount St Helens and Mount Adams inferred from magnetotelluric data. Nature Geoscience, 2(11), 785-789.
- Hirose, K. (2002). Phase transitions in pyrolitic mantle around 670-km depth: Implications for upwelling of plumes from the lower mantle. Journal of Geophysical Research: Solid Earth, 107(B4), ECV-3.

- Huang, Q., Schmerr, N., Waszek, L., & Beghein, C. (2019). Constraints on seismic anisotropy in the mantle transition zone from long-period SS precursors. Journal of Geophysical Research: Solid Earth, 124(7), 6779-6800.
- Inoue, T., Irifune, T., Higo, Y., Sanehira, T., Sueda, Y., Yamada, A., ... & Utsumi, W. (2006). The phase boundary between wadsleyite and ringwoodite in Mg2SiO4 determined by in situ X-ray diffraction. Physics and Chemistry of Minerals, 33(2), 106-114.
- Inoue, T., Wada, T., Sasaki, R., & Yurimoto, H. (2010). Water partitioning in the Earth's mantle. Physics of the Earth and Planetary Interiors, 183(1-2), 245-251.
- Ishii, T., Kojitani, H. and Akaogi, M., (2018). Phase relations and mineral chemistry in pyrolitic mantle at 1600–2200° C under pressures up to the uppermost lower mantle: Phase transitions around the 660-km discontinuity and dynamics of upwelling hot plumes. Physics of the Earth and Planetary Interiors, 274, pp.127-137.
- Ishii, T., Kojitani, H., & Akaogi, M. (2019). Phase Relations of Harzburgite and MORB up to the Uppermost Lower Mantle Conditions: Precise Comparison With Pyrolite by Multisample Cell High-Pressure Experiments With Implication to Dynamics of Subducted Slabs. Journal of Geophysical Research: Solid Earth, 124(4), 3491-3507.
- Ita, J., & Stixrude, L. (1992). Petrology, elasticity, and composition of the mantle transition zone. Journal of Geophysical Research: Solid Earth, 97(B5), 6849-6866.
- Julià, J., & Nyblade, A. A. (2013). Probing the upper mantle transition zone under Africa with P520s conversions: Implications for temperature and composition. Earth and Planetary Science Letters, 368, 151-162.
- Katsura, T., Yamada, H., Nishikawa, O., Song, M., Kubo, A., Shinmei, T., ... & Funakoshi, K. I. (2004). Olivine-wadsleyite transition in the system (Mg, Fe) 2SiO4. Journal of Geophysical Research: Solid Earth, 109(B2).
- Katsura, T., Yoneda, A., Yamazaki, D., Yoshino, T., & Ito, E. (2010). Adiabatic temperature profile in the mantle. Physics of the Earth and Planetary Interiors, 183(1-2), 212-218.
- Kawazoe, T., Ohuchi, T., Nishihara, Y., Nishiyama, N., Fujino, K., & Irifune, T. (2013). Seismic anisotropy in the mantle transition zone induced by shear deformation of wadsleyite. Physics of the Earth and Planetary Interiors, 216, 91-98.
- Kennett, B. L., Engdahl, E. R., & Buland, R. (1995). Constraints on seismic velocities in the Earth from traveltimes. Geophysical Journal International, 122(1), 108-124.
- Király, Á., Portner, D. E., Haynie, K. L., Chilson-Parks, B. H., Ghosh, T., Jadamec, M., et al., (2020). The effect of slab gaps on subduction dynamics and mantle upwelling. Tectonophysics, 785, 228458.
- Kiser, E., Levander, A., Zelt, C., Schmandt, B., & Hansen, S. (2018). Focusing of melt near the top of the Mount St. Helens (USA) magma reservoir and its relationship to major volcanic eruptions. Geology, 46(9), 775-778.
- Kiser, E., Palomeras, I., Levander, A., Zelt, C., Harder, S., Schmandt, B., ... & Ulberg, C. (2016). Magma reservoirs from the upper crust to the Moho inferred from high-resolution Vp and Vs models beneath Mount St. Helens, Washington State, USA. Geology, 44(6), 411-414.
- Klein, F. W. (1985). User's guide to HYPOINVERSE, a program for VAX and Professional 350 computers to solve for earthquake locations (No. 85-515). US Geological Survey,.

- Kong, F., Gao, S.S., Liu, K.H., Song, J., Ding, W., Fang, Y., Ruan, A., & Li, J. (2018). Receiver function investigations of seismic anisotropy layering beneath Southern California. Journal of Geophysical Research: Solid Earth, 123(12), 10-672.
- Lawrence, J. F., & Shearer, P. M. (2006). A global study of transition zone thickness using receiver functions. Journal of Geophysical Research: Solid Earth, 111(B6).
- Lay, T., Williams, Q., & Garnero, E. J. (1998). The core–mantle boundary layer and deep Earth dynamics. Nature, 392(6675), 461-468.
- Lebedev, S., Chevrot, S., & van der Hilst, R. D. (2002). Seismic evidence for olivine phase changes at the 410-and 660-kilometer discontinuities. Science, 296(5571), 1300-1302.
- Lees, J. M., & Crosson, R. S. (1989). Tomographic inversion for three-dimensional velocity structure at Mount St. Helens using earthquake data. Journal of Geophysical Research: Solid Earth, 94(B5), 5716-5728.
- Lehto, H. L., Roman, D. C., & Moran, S. C. (2010). Temporal changes in stress preceding the 2004–2008 eruption of Mount St. Helens, Washington. Journal of Volcanology and Geothermal Research, 198(1-2), 129-142.
- Lehto, H. L., Roman, D. C., & Moran, S. C. (2013). Source mechanisms of persistent shallow earthquakes during eruptive and non-eruptive periods between 1981 and 2011 at Mount St. Helens, Washington. Journal of volcanology and geothermal research, 256, 1-15.
- Levin, V., & Park, J. (1997). P-SH conversions in a flat-layered medium with anisotropy of arbitrary orientation. Geophysical Journal International, 131(2), 253-266.
- Lipman, P. W. & Mullineaux, D. R. (Eds.) (1981). The 1980 Eruptions of Mount St. Helens, Washington. U.S. Geological Survey Professional Paper , 1250, 844 p., 1 plate.
- Liu, K.H., Elsheikh, A., Lemnifi, A., Purevsuren, U., Ray, M., Refayee, H., et al., (2014). A uniform database of teleseismic shear wave splitting measurements for the western and central United States. Geochemistry, Geophysics, Geosystems, 15(5), 2075-2085.
- Liu, L., & Stegman, D. R. (2011). Segmentation of the Farallon slab. Earth and Planetary Science Letters, 311(1-2), 1-10.
- Long, M. D., & Silver, P. G. (2009). Shear wave splitting and mantle anisotropy: Measurements, interpretations, and new directions. Surveys in Geophysics, 30(4), 407-461.
- Long, M. D., Becker, T. W. (2010). Mantle dynamics and seismic anisotropy. Earth and Planetary Science Letters, 297(3-4), 341-354.
- Long, M.D., Till, C.B., Druken, K.A., Carlson, R.W., Wagner, L.S., Fouch, M.J., et al., (2012). Mantle dynamics beneath the Pacific Northwest and the generation of voluminous back-arc volcanism. Geochemistry, Geophysics, Geosystems, 13(8).
- Lynner, C., & Long, M. D. (2015). Heterogeneous seismic anisotropy in the transition zone and uppermost lower mantle: evidence from South America, Izu-Bonin and Japan. Geophysical Journal International, 201(3), 1545-1552.
- Mainprice, D. (2015) Seismic anisotropy of the deep Earth from a mineral and rock physics perspective. Treatise in Geophysics, 2nd Edition, Volume 2, 487-538
- Malone, S. D., Boyko, C., & Weaver, C. S. (1983). Seismic precursors to the Mount St. Helens eruptions in 1981 and 1982. Science, 221(4618), 1376-1378.

- Mercier, J. P., Bostock, M. G., & Baig, A. M. (2006). Improved Green's functions for passive-source structural studies. Geophysics, 71(4), SI95-SI102.
- Mohiuddin, A., Karato, S. I., & Girard, J. (2020). Slab weakening during the olivine to ringwoodite transition in the mantle. Nature Geoscience, 13(2), 170-174.
- Mondal, P., & Long, M. D. (2020). Strong seismic anisotropy in the deep upper mantle beneath the Cascadia backarc: Constraints from probabilistic finite-frequency SKS splitting intensity tomography. Earth and Planetary Science Letters, 539, 116172.
- Montagner, J. P., Griot-Pommera, D. A., & Lavé, J. (2000). How to relate body wave and surface wave anisotropy?. Journal of Geophysical Research: Solid Earth, 105(B8), 19015-19027.
- Moran, S. C. (1994). Seismicity at Mount St. Helens, 1987–1992: Evidence for repressurization of an active magmatic system. Journal of Geophysical Research: Solid Earth, 99(B3), 4341-4354.
- Morgan, S. C., Malone, S. D., Qamar, A. I., Thelen, W. A., Wright, A. K., & Caplan-Auerbach, J. (2008). Seismicity associated with renewed dome building at Mount St. Helens, 2004-2005 (No. 1750-2, pp. 27-60). US Geological Survey.
- Munch, F. D., Grayver, A. V., Kuvshinov, A., & Khan, A. (2018). Stochastic inversion of geomagnetic observatory data including rigorous treatment of the ocean induction effect with implications for transition zone water content and thermal structure. Journal of Geophysical Research: Solid Earth, 123(1), 31-51.
- Musumeci, C., Gresta, S., & Malone, S. D. (2002). Magma system recharge of Mount St. Helens from precise relative hypocenter location of microearthquakes. Journal of Geophysical Research: Solid Earth, 107(B10), ESE-16.
- Neuberg, J., & Pointer, T. (2000). Effects of volcano topography on seismic broad-band waveforms. Geophysical Journal International, 143(1), 239-248.
- Ohuchi, T., Fujino, K., Kawazoe, T., & Irifune, T. (2014). Crystallographic preferred orientation of wadsleyite and ringwoodite: Effects of phase transformation and water on seismic anisotropy in the mantle transition zone. Earth and Planetary Science Letters, 397, 133-144.
- Pallister, J. S., Thornber, C. R., Cashman, K. V., Clynne, M. A., Lowers, H., Mandeville, C. W., ... & Meeker, G. P. (2008). Petrology of the 2004-2006 Mount St. Helens lava dome--Implications for magmatic plumbing and eruption triggering (No. 1750-30, pp. 647-702). US Geological Survey.
- Pesicek, J. D., Wellik, J. J., Prejean, S. G., & Ogburn, S. E. (2018). Prevalence of seismic rate anomalies preceding volcanic eruptions in Alaska. Frontiers in Earth Science, 6, 100.
- Rawlinson, N., & Sambridge, M. (2004). Wave front evolution in strongly heterogeneous layered media using the fast marching method. Geophysical Journal International, 156(3), 631-647.
- Ritterbex, S., Carrez, P., & Cordier, P. (2020). Deformation across the mantle transition zone: A theoretical mineral physics view. Earth and Planetary Science Letters, 547, 116438.
- Roman, D. C., & Cashman, K. V. (2018). Top–down precursory volcanic seismicity: implications for 'stealth' magma ascent and long-term eruption forecasting. Frontiers in Earth Science, 6, 124.

- Saikia, A., Frost, D. J., & Rubie, D. C. (2008). Splitting of the 520-kilometer seismic discontinuity and chemical heterogeneity in the mantle. Science, 319(5869), 1515-1518.
- Satta, N., Marquardt, H., Kurnosov, A., Buchen, J., Kawazoe, T., McCammon, C., & Ballaran, T. B. (2019). Single-crystal elasticity of iron-bearing phase E and seismic detection of water in Earth's upper mantle. American Mineralogist, 104(10), 1526-1529.
- Schmandt, B., & Humphreys, E. (2011). Seismically imaged relict slab from the 55 Ma Siletzia accretion to the northwest United States. Geology, 39(2), 175-178.
- Schmandt, B., & Lin, F. C. (2014). P and S wave tomography of the mantle beneath the United States. Geophysical Research Letters, 41(18), 6342-6349.
- Schmandt, B., Thomas, A., & Thelen, W.. (2017). Mount St. Helens 3C Node Array [Data set]. International Federation of Digital Seismograph Networks. https://doi.org/10.7914/SN/YI_2017
- Seton, M., Müller, R.D., Zahirovic, S., Gaina, C., Torsvik, T., Shephard, G., Talsma, A., Gurnis, M., Turner, M., Maus, S. and Chandler, M., (2012). Global continental and ocean basin reconstructions since 200 Ma. Earth-Science Reviews, 113(3-4), pp.212-270.
- Shapiro, N. M., Droznin, D. V., Droznina, S. Y., Senyukov, S. L., Gusev, A. A., & Gordeev, E. I. (2017). Deep and shallow long-period volcanic seismicity linked by fluid-pressure transfer. Nature Geoscience, 10(6), 442-445.
- Shearer, P. M. (1996). Transition zone velocity gradients and the 520-km discontinuity. Journal of Geophysical Research: Solid Earth, 101(B2), 3053-3066.
- Shen, W., Ritzwoller, M. H., Schulte-Pelkum, V., & Lin, F. C. (2013). Joint inversion of surface wave dispersion and receiver functions: a Bayesian Monte-Carlo approach. Geophysical Journal International, 192(2), 807-836.
- Sinogeikin, S. V., Bass, J. D., & Katsura, T. (2003). Single-crystal elasticity of ringwoodite to high pressures and high temperatures: implications for 520 km seismic discontinuity. Physics of the Earth and Planetary Interiors, 136(1-2), 41-66.
- Suzuki, A., Ohtani, E., Morishima, H., Kubo, T., Kanbe, Y., Kondo, T., ... & Kikegawa, T. (2000). In situ determination of the phase boundary between wadsleyite and ringwoodite in Mg2SiO4. Geophysical Research Letters, 27(6), 803-806.
- Swanson, D. A., Casadevall, T. J., Dzurisin, D., Malone, S. D., Newhall, C. G., & Weaver, C. S. (1983). Predicting eruptions at Mount St. Helens, June 1980 through December 1982. Science, 221(4618), 1369-1376.
- Thelen, W. A., Crosson, R. S., & Creager, K. C. (2008). Absolute and relative locations of earthquakes at Mount St. Helens, Washington using continuous data: Implications for magmatic processes. In A Volcano Rekindled: The Renewed Eruption of Mount St. Helens, 2004–2006 (Vol. 1750, pp. 71-95). Denver, Colo: US Geological Survey.
- Tian, D., Lv, M., Wei, S. S., Dorfman, S. M., & Shearer, P. M. (2020). Global variations of Earth's 520-and 560-km discontinuities. Earth and Planetary Science Letters, 552, 116600.
- Tsujino, N., Yoshino, T., Yamazaki, D., Sakurai, M., Sun, W., Xu, F., ... & Higo, Y. (2019). Phase transition of wadsleyite-ringwoodite in the Mg2SiO4-Fe2SiO4 system. American Mineralogist: Journal of Earth and Planetary Materials, 104(4), 588-594.
- U.S. Geological Survey, 2017, 1 Arc-second Digital Elevation Models (DEMs) - USGS National Map 3DEP Downloadable Data Collection: U.S. Geological Survey.

- Ulberg, C. W., Creager, K. C., Moran, S. C., Abers, G. A., Thelen, W. A., Levander, A., ... & Crosson, R. S. (2020). Local source Vp and Vs tomography in the Mount St. Helens region with the iMUSH broadband array. Geochemistry, Geophysics, Geosystems, 21(3), e2019GC008888.
- Van Keken, P. E., Karato, S., & Yuen, D. A. (1996). Rheological control of oceanic crust separation in the transition zone. Geophysical Research Letters, 23(14), 1821-1824.
- Vinnik, L., & Montagner, J. P. (1996). Shear wave splitting in the mantle Ps phases. Geophysical Research Letters, 23(18), 2449-2452.
- Wagner, L. S., & Long, M. D. (2013). Distinctive upper mantle anisotropy beneath the High Lava Plains and Eastern Snake River Plain, Pacific Northwest, USA. Geochemistry, Geophysics, Geosystems, 14(10), 4647-4666
- Waite, G. P., & Moran, S. C. (2009). VP Structure of Mount St. Helens, Washington, USA, imaged with local earthquake tomography. Journal of Volcanology and Geothermal Research, 182(1-2), 113-122.
- Walsh, E., Arnold, R., & Savage, M. K. (2013). Silver and Chan revisited. Journal of Geophysical Research: Solid Earth, 118(10), 5500-5515.
- Wang, F., Barklage, M., Lou, X., van der Lee, S., Bina, C. R., & Jacobsen, S. D. (2018). HyMaTZ: a Python program for modeling seismic velocities in hydrous regions of the mantle transition zone. Geochemistry, Geophysics, Geosystems, 19(8), 2308-2324.
- Wang, R., Schmandt, B., Zhang, M., Glasgow, M., Kiser, E., Rysanek, S., & Stairs, R. (2020). Injection-induced earthquakes on complex fault zones of the Raton Basin illuminated by machine-learning phase picker and dense nodal array. Geophysical Research Letters, 47(14), e2020GL088168.
- Waszek, L., Tauzin, B., Schmerr, N. C., Ballmer, M. D., & Afonso, J. C. (2021). A poorly mixed mantle transition zone and its thermal state inferred from seismic waves. Nature Geoscience, 14(12), 949-955.
- Weaver, C.S., Grant, W.G., Malone, S.D., and Endo, E.T., (1981), Post-May 18 seismicity; volcanic and tectonic implications. US Geol. Surv. Prof. Pap, 1250, p. 109–121.
- Wu, W., Ni, S., & Irving, J. C. (2019). Inferring Earth's discontinuous chemical layering from the 660-kilometer boundary topography. Science, 363(6428), 736-740.
- Xu, W., Lithgow-Bertelloni, C., Stixrude, L., & Ritsema, J. (2008). The effect of bulk composition and temperature on mantle seismic structure. Earth and Planetary Science Letters, 275(1-2), 70-79.
- York, D., Evensen, N. M., Martınez, M. L., & De Basabe Delgado, J. (2004). Unified equations for the slope, intercept, and standard errors of the best straight line. American journal of physics, 72(3), 367-375.
- Yuan, K., & Beghein, C. (2013). Seismic anisotropy changes across upper mantle phase transitions. Earth and Planetary Science Letters, 374, 132-144
- Zhang, J. S., & Bass, J. D. (2016). Sound velocities of olivine at high pressures and temperatures and the composition of Earth's upper mantle. Geophysical Research Letters, 43(18), 9611-9618.

- Zhang, J. S., Bass, J. D., & Schmandt, B. (2018). The elastic anisotropy change near the 410-km discontinuity: Predictions from single-crystal elasticity measurements of olivine and wadsleyite. Journal of Geophysical Research: Solid Earth, 123(4), 2674-2684.
- Zhou, Q., Hu, J., Liu, L., Chaparro, T., Stegman, D. R., & Faccenda, M. (2018). Western US seismic anisotropy revealing complex mantle dynamics. Earth and Planetary Science Letters, 500, 156-167.
- Zhou, W. Y., Zhang, J. S., Huang, Q., Lai, X., Chen, B., Dera, P., & Schmandt, B. (2022). High pressure-temperature single-crystal elasticity of ringwoodite: Implications for detecting the 520 discontinuity and metastable ringwoodite at depths greater than 660 km. Earth and Planetary Science Letters, 579, 117359
- Zhu, H., Li, X., Yang, J., Stern, R. J., & Lumley, D. E. (2020). Poloidal-and toroidal-mode mantle flows underneath the Cascadia Subduction Zone. Geophysical Research Letters, e2020GL087530.